



CHALMERS
UNIVERSITY OF TECHNOLOGY



UNIVERSITY OF GOTHENBURG



Test System to Evaluate Energy-Harvesting Technologies for Wireless Sensors

Master's thesis in Embedded Electronic System Design

KJARTAN BJARNI KRISTJÁNSSON
STEINAR ÞORVALDSSON

Test System to Evaluate Energy-Harvesting Methods for Wireless Sensors
KJARTAN BJARNI KRISTJÁNSSON
STEINAR ÞORVALDSSON

© KJARTAN B. KRISTJÁNSSON and STEINAR ÞORVALDSSON, 2016.

Examiner: PER LARSSON-EDEFORS
Academic supervisor: LENA PETERSON
Company supervisor: MARTIN GEORGE

Department of Computer Science and Engineering
Chalmers University of Technology
SE - 412 96 Göteborg
Sweden
Telephone +46 (0)31-772 1000

Cover: The Athol hardware mounted on a Raspberry Pi

Department of Computer Science and Engineering
Göteborg, Sweden 2016

Abstract

Wireless sensor networks are rapidly growing, both in number and size, and powering their parts with batteries or wires has become difficult. Energy-harvesting is a possible way to power the sensors, which are often located in environments where harvest-able energy sources are present, such as vibration or radio-waves. However, verifying that an energy-harvesting method is capable of sustaining a wireless sensor is not trivial and using conventional lab equipment for testing the viability of an energy-harvesting method on-site is not always possible due to spatial restrictions.

In this thesis, a lightweight, but precise test system to evaluate energy harvesting technologies for wireless sensors is presented. We describe and discuss the test system's specification, from the general characteristic of energy-harvesting, to wireless sensor systems. Furthermore, details about the design are revealed and the results from testing and evaluation are presented.

The system designed was capable of drawing controlled power levels and emulating wireless sensors, mimicking their power architecture interface to energy-harvesting systems. This was done with accuracy of within 5% deviation for currents from $1\ \mu\text{A}$ up to 250 mA, with $< 1\%$ average relative accuracy over the entire range, a range that was deemed sufficient to accurately emulate most wireless sensors. The test system turned out small enough to be hand-held and is therefore easily installed in the field.

The system turned out to be useful for evaluating a piezo-electric harvesting system, and our analysis indicates that the general-purpose nature of the system should make it useful for evaluating other harvesting technologies, suitable for wireless sensors, such as radio-frequency and electromagnetic energy-harvesting.

Keywords: Wireless Sensor Networks, Energy-Harvesting, Evaluation System, Piezo-Electric Energy-Harvesting

Nomenclature

AC	Alternating Current
ADC	Analog-to-Digital Converter
ASIC	Application-Specific Integrated Circuit
DAC	Digital-to-Analog Converter
DC	Direct Current
EM	Electro-Magnetic
GPIO	General-Purpose Input/Output
GUI	Graphical User Interface
I ² C	Inter-Integrated Circuit
IC	Integrated Circuit
MPPT	Maximum Power Point Tracking
MVC	Model-View-Controller
PVDF	Polyvinylidene Fluoride
PZT	Lead Zirconate Titanate
RF	Radio-Frequency
SNR	Signal-to-Noise Ratio
SPI	Serial Peripheral Interface
WSN	Wireless Sensor Network

Contents

1	Introduction	6
1.1	Background	6
1.2	Purpose	7
1.3	Limitations	7
1.4	Delimitations	8
2	Theory - WSNs and Energy-Harvesting	9
2.1	Wireless Sensor Networks	9
2.2	Energy-Harvesting	10
2.2.1	Piezo-Electric Harvesting	11
2.2.2	Electro-magnetic Harvesting	13
2.2.3	Radio-Frequency	13
3	Theory - Circuit Elements	15
3.1	Current Mirrors	15
3.2	Trans-conductance Amplifiers	16
3.3	Data Converters	17
4	Pre-Study	20
4.1	Piezo-Electric Harvesting	20
4.1.1	Viability	20
4.2	Electro-Magnetic Harvesting	20
4.2.1	Viability	21
4.3	Radio-Frequency Harvesting	21
4.4	Viability	21
4.5	Specification Synthesis	22
4.5.1	Use Cases	22
4.5.2	Proposed Capability	23
4.5.3	Sensor Emulation	23
4.5.4	System Characterisation	24
4.5.5	Material Characterisation	24
4.5.6	Maximum Input Voltage	24
4.5.7	Minimum Input Voltage	25
4.5.8	Minimum Current	25
4.5.9	Maximum Current	25
4.5.10	Power	26
4.5.11	Leakage	26
4.5.12	Accuracy	26
4.5.13	Bandwidth and Response Time	26
4.6	Final Specification	26

5	System Design and Validation Method	28
5.1	Implementation	28
5.1.1	Hardware: Overview	28
5.1.2	Hardware: ADC	29
5.1.3	Hardware: DAC	30
5.1.4	Hardware: micro-cell	31
5.1.5	Hardware: macro-cell	33
5.1.6	Software: Overview and Architecture	34
5.1.7	Software: Functionality	35
5.2	Validation Method	37
6	Results	38
6.1	ADC	38
6.2	Macro-Cell	40
6.3	Micro-Cell With Mirror	42
6.4	Micro-Cell Without Mirror	45
6.5	Calibrated Results	48
6.6	Leakage Current	50
6.7	Rise and Fall Time	50
6.8	Timing Jitter	51
6.9	Power Integration	52
6.10	Summary	53
6.11	Evaluation of a Energy-Harvesting System	53
6.11.1	Piezo-Electric Material and The Drill	53
6.11.2	Piezo-electric Material on a Vibration Table	56
7	Discussion	61
7.1	Current-Mirror Performance	61
7.2	Load-cells Combined	61
7.3	Minimum Input Voltage - Current Foldback	62
7.4	Calibration	62
7.5	Timing Jitter	63
7.6	Total Power Calculations	63
8	Conclusion	64
9	Future Work	65
9.1	Improving Jitter to Improve Speed	65
9.2	Potential For Higher Resolution	65
9.3	Constant Voltage Mode	65
9.4	Generalisation of the Thesis Work	66
	References	67

A	Calculations and Derivations	70
A.1	ADC	70
A.1.1	Resolution	70
A.1.2	Noise and SNR	70
A.1.3	Offset Error	70
A.2	DAC	71
A.2.1	Noise	71
A.2.2	Voltage reference	71
A.3	Loadcells	71
A.3.1	Micro-cell - Dynamic Range	71
A.3.2	Macro-cell - Dynamic Range	72

1 Introduction

The thesis topic was proposed by the company Syntronic [1], but adapted by the authors to fit the scope of a master thesis. Syntronic is a consulting company in the area of embedded hardware systems, including radio and embedded software. More and more wireless sensors are being introduced into systems for their clients in an area where power sourcing and efficiency is increasingly important. Batteries and solar cells are not always the best solution; batteries degrade and require eventual replacement and solar cells do not produce energy at night. Here other energy-harvesting systems than solar energy-harvesting for battery-less designs come in as a strong candidate to replace batteries. Syntronic proposed the design of a test system to evaluate current and upcoming piezoelectric and electromagnetic energy-harvesting technologies to power wireless sensors by vibration, rotation or electromagnetic energy-harvesting.

There are numerous experiments that a designer for energy-harvesting wireless sensors might want to perform when designing energy-harvesting systems, both on energy-harvesting materials and complete harvesters of different kinds. Furthermore, emulation of the interaction between a energy-harvester and the wireless sensor subsystem it powers could bring insight into stability and viability and serve as an important part of the design validation process.

1.1 Background

The technology environment of this essay is the IoT (Internet of Things) type of devices; low-power, wireless and battery-less devices. These devices are often powered by batteries. Recently, however, solutions based on energy-harvesting in conjunction with supercapacitors are showing promise with decreasing energy consumption of embedded microcomputers. The most prominent channel of energy-harvesting is piezo-electric energy-harvesting, which harvests kinetic energy from the environment. This type of energy-harvesting is particularly effective in industrial settings due to the presence of vibrating machinery [2]. Another channel that shows promise is harvesting of intentional or ambient electromagnetic radiation [3], which is a method which has been emerging lately as a potentially viable energy-harvesting source [4]. There are also other energy-harvesting channels available such as solar and thermal, but piezo-electric and electromagnetic sources are of primary interest in this thesis, due to potential applications in industry and society where solar or thermal is not applicable [5].

For wireless battery-less sensors and systems, there needs to be a way to verify that energy-harvesting offerings and supporting designs can supply long-term energy and store enough short-term energy to fulfill the requirements of wireless sensor nodes with complex load profiles. Moreover, the environment they harvest from can usually not be brought to the lab for testing, and their applicational validity depends on the environmental excitation they eventually reside in. Hauling in conventional lab equipment for field testing energy-harvesting system is not feasible either, due to its weight and size. Mobility and in-field testing are therefore important aspects of evaluating energy-harvesting systems.

Ethical aspects may arise as well, where if wireless systems are used in sensitive applications such as military, aerospace, medical or life-critical, then they need to be validated thoroughly to function in their energy-harvesting environment. Specialised evaluation systems may play an important role here in providing reliability data to certify that they can be powered, and function as expected where they are to be deployed.

Sustainability is highly regarded today as a countering force to global warming and pollution. One arm of sustainable development is increasing efficiency of devices and reduced reliance on harmful chemicals and energy generated by burning fossil fuels. Harvesting energy through vibration or ambient radio-frequency radiation indirectly increases efficiency in the modern society. Enabling the development of energy-harvesting electronics can directly aid sustainable development and help tackle environmental concerns.

Today it is not possible to find available commercial test systems for purchase addressing all of the issues raised here and literature investigating the evaluation of energy-harvesting systems in practice and in this context was not found.

1.2 Purpose

The purpose of this essay is to explore, design and implement a test system capable of evaluating energy-harvesting systems, with mobility in mind.

The essay goals are to derive what the requirements and specifications are for such a system; to design and implement a system that fully or closely fulfils the requirements and the specification; to verify that the built system conforms to the specification and finally, to have it evaluate an energy-harvesting component to gauge its usefulness in a real application.

The research questions of the essay are the following:

1. What common characteristics are present when piezo-electric, electromagnetic and radio-frequency energy-harvesting methods are used to power wireless sensors?
2. What are the requirements and specification of a system capable of evaluating the energy-harvesting systems mentioned above, when they are used to power wireless sensors?
3. How does such a system perform when implemented according to the specification derived as part of question 2?

1.3 Limitations

The current consumption of a wireless sensor easily spans many decades in amplitude, from sleep current to active mode current. An example is Texas Instruments' CC2640 [6], with $1\ \mu\text{A}$ standby mode and $12\ \text{mA}$ active mode consumption when transmitting wirelessly. Controlling extremely low currents for the purpose of emulating a wireless sensor or evaluating an energy-harvester is

challenging. As the thesis work is constrained by time and budget it runs into design limitations and technological limitations at these low currents, which may limit the capability to reach the targeted specification that covers all desired features. At the lower current range, where active devices may be operating in the sub-threshold region, many practical issues arise with impedance matching and designs that require a custom-level application-specific integrated circuit (ASIC) solution to handle.

Due to the matching problem, and relative rarity of matched devices available in the form of widely available ICs (Integrated Circuits), the design may be limited by scarce offering of required parts.

1.4 Delimitations

There are several energy-harvesting methods in addition to those that have been listed above, such as solar energy-harvesting and thermoelectric harvesting. They will, however, not be evaluated in this thesis since they are in many cases not as interesting for use with wireless sensors due to environmental limitations, even though in practice they could be evaluated and used in some applications. The scope has been limited to the methods deemed most interesting and suitable for use with wireless sensors by the authors. The time span and budget of the thesis also contributes to this decision.

2 Theory - WSNs and Energy-Harvesting

This chapter is about the theory behind wireless sensors networks and the energy-harvesting methods that are most suitable for use with wireless sensors. They are covered as they are the systems the design of this thesis is meant to be able to evaluate.

2.1 Wireless Sensor Networks

Wireless sensor networks (WSN) are applicable in many commercial applications and are rapidly growing in size [7]. As a result of the growing size of the networks, powering the sensors has become troublesome. Small-scale batteries that are available today have low energy densities and need to be replaced regularly at a service cost, which is infeasible for networks that have more than a few nodes or when the nodes are in areas which are physically hard to reach such as inside concrete [8] [9]. Another shortcoming of batteries is that their operational temperature is typically within the range $25 \pm 60^\circ\text{C}$ which may be insufficient in some applications [10]. Powering individual sensors using electrical wiring is expensive and very inconvenient if there are more than a handful of sensors or if they are spread over a large area.

An alternative way of powering network nodes is to harvest energy from their immediate environment to power the nodes directly or to charge some kind of a storage element that powers the nodes [8] [9]. Harvesting energy from the environment is a challenge because the environment can be very dynamic and changing, and variations in placement, design-specific details and activity duty cycles can affect the capability of the whole system when assembled to fulfill availability requirements [3].

It is obvious that in order to maximise the time sensors can function, or stay online while being powered by any limited or low power energy source, sensors need to be conservative with the energy they use. They need to use the energy efficiently by making the most out of the energy available, such as by utilising as low currents and voltages as possible to function while running, since power consumed is the product of the two. Another option is to turn off or almost so when not sensing or performing calculations.

When battery-less and wireless energy-harvesting designs need to store energy locally, the traditional way to do so is with a capacitor, mechanical methods might be possible, but evidence for practical ways to achieve it at embedded sensor scale was not found, possibly because they might not be practical considering the lack of research material available. Without an energy buffer, such as a capacitor, a sudden drop in produced energy by a harvester, or the wireless sensor drawing power exceeding the generation capability, would cause a sensor to malfunction. For this reason it can be deduced that most wireless sensors based on energy-harvesting systems will utilise an energy buffer of some sort between the energy-harvester itself and the load. That is, long term energy is stored in a reservoir for absorbing short stints of energy levels exceeding the generation capability of the harvester. In this thesis essay, we will assume that

in the near future such a buffer will be a capacitor due to practical reasons.

The equation for energy stored in a capacitor, $\frac{CV^2}{2}$, hints that increasing the voltage is the most efficient way to store energy in a capacitor due to the square law. Capacitors tend to get bigger as the capacitance is increased, reducing their usefulness in small wireless designs. Based on that and the previous discussion, a battery-less design will attempt to minimise the voltage powering the sensor circuitry, while maximising the voltage supported by the energy storage node. A DC-DC converter can then efficiently convert the higher voltages in the storage node to a regulated lower voltage on the sensor side to keep the voltage low there. So a typical system arrangement, based on the discussion may look something like Fig. 1.

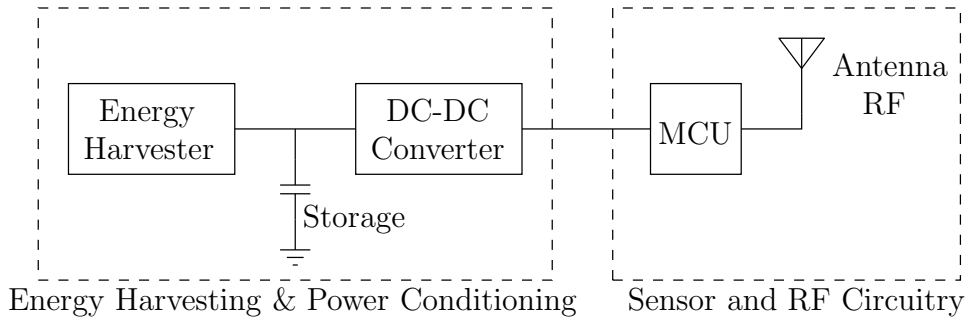


Figure 1: System arrangement for a wireless sensor that is powered by an energy-harvester

A setup like this will function until the voltage on the storage capacitor falls below the capability of the DC/DC converter to regulate the output voltage side, which is the sensor side. The usable energy range is the difference in energy stored between the lowest and highest possible system voltages on the storage capacitor. It is clear that in order for a sensor to function indefinitely from an energy-harvesting source, the condition must exist that the average harvester power must exceed the average power consumed by the sensor. With an energy buffer, the power consumed by the sensor can exceed the average harvesting rate temporarily, until the capacitor voltage falls below the point guaranteeing system functionality. From this we can deduce that by monitoring the storage node, knowing the value of the capacitance there, we can estimate the performance of an energy-harvester powering a wireless sensor. Monitoring the node can yield the margins from total system malfunction or how much energy is left in the storage capacitor at all times.

2.2 Energy-Harvesting

There are various energy-harvesting technologies available but not all of them are suitable for use with wireless sensors. Sensors are often located in areas that are neither exposed permanently to strong sunlight nor to high temperature

gradients, effectively ruling out technologies such as solar energy-harvesting and thermoelectric harvesting.

The following subsections contain theory on the energy-harvesting methods that are most suitable for use with wireless sensors as well as the reasons for their suitability.

2.2.1 Piezo-Electric Harvesting

Piezo-electric materials are materials that have the ability to produce an electrical charge proportional to the mechanical stress applied to them [11]. A diagram that shows the behaviour of such a material can be seen in Fig. 2. When the system is in a steady state (diagram *a*), the molecules within the materials are electrically neutral, irrespective of the force applied to the material. When a force, F , is applied and the material is being deformed (diagram *b*), the molecules within the material become polarised and an electric field is formed. This electric field causes the free charges in the conductor to flow within. The flow continues until the polarisation effect is neutralised. When the force is released, the reverse occurs and charge flows in the opposite direction [12].

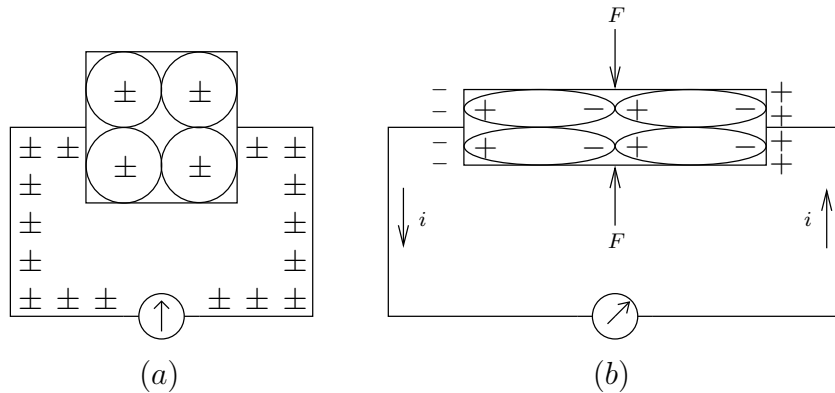


Figure 2: Behaviour of piezo-electric material under mechanical stress (reproduced from [12])

The most common setup that makes use of this technology consists of a cantilever (supported beam) that is a sandwich of layers of piezo-electric plates, possibly separated by supporting materials.

There are many materials that have piezo-electric properties but the ones that are most commonly used in practice are called Lead zirconate titanate (PZT) and Polyvinylidene fluoride (PVDF) [13]. There are some advantages and disadvantages in choosing either one. PZT yields more power but is brittle and therefore breaks if it is deformed too much. PVDF is less expensive and has greater reliability but gives less power.

At the circuit level, a single piezo-electric material element is electronically

modeled as a voltage source, in series with a capacitor and a resistor, as seen in Fig. 3. When the material is stressed, an open-circuit voltage develops across the voltage source. When a load is attached, AC excitation energy flows from the element into the loading impedance [13]. Piezo-electric energy-harvesting generally yields high voltage levels but low currents [2].

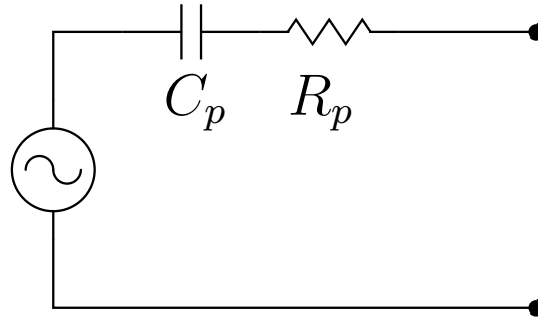


Figure 3: Circuit model of a piezo-electric material

Note the particular arrangement of the circuit model, namely the series capacitor, implying that only alternating voltages can pass. Fast transients and sinusoidal excitations can be harvested for energy but the energy is not stored in the piezo-electric material itself. Instead, it is stored in a capacitor-like mechanism which is connected in parallel with the material. So in practice, when these materials are used for energy-harvesting, a rectifier and a storage element such as a capacitor are used to create usable DC voltages as shown in Fig. 4.

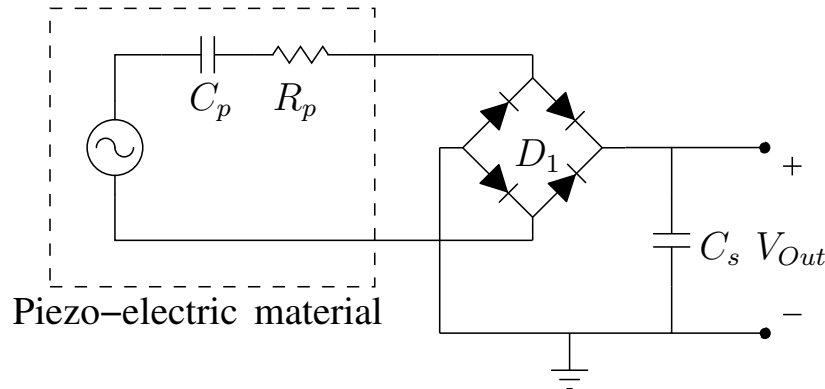


Figure 4: Harvesting circuit for piezo-electric harvesting

2.2.2 Electro-magnetic Harvesting

Electro-magnetic (EM) energy conversion is well known in electric motors. Less known, but of interest for wireless sensors, is the use of coils and moving magnets, i.e. electromagnetic induction, to harvest energy from mechanical vibrations [8]. Vibrational energy-harvesting through these means is of interest to wireless sensors.

A magnet that is excited by environmental vibrations is made to oscillate through a coil that forms a primary winding of a transformer. This converts mechanical motion to electrical energy that can be harvested on the secondary transformer winding.

At the circuit level, electro-magnetic energy-harvesting is modeled by a transformer winding where energy is introduced in the form of a voltage across the terminals when excitation takes place. This voltage needs to be rectified and stored to be converted into usable energy for powering systems, as demonstrated in Fig. 5. Electro-magnetic energy-harvesting methods generally yield high currents but low voltage levels [2].

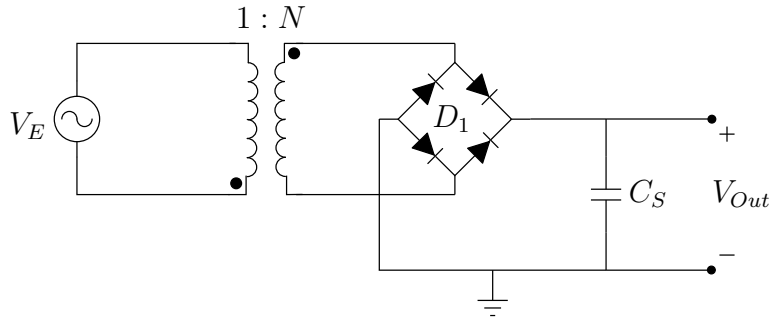


Figure 5: Electromagnetic energy-harvesting circuit

For maximum power output for a resonant electro-magnetic harvester such as the one described above, the excitation vibration frequency should match the mechanical resonance frequency of the setup [2].

Wireless sensors are often placed in areas where strict size constraints apply. Electro-magnetic energy-harvesting systems tend to be bulkier than their competing technologies which use other methods to harvest energy so they might not be applicable in every situation [2] [8].

2.2.3 Radio-Frequency

Radio-frequency (RF) energy-harvesting is the act of harvesting energy from RF waves that are radiating through space. Those waves can be from a source that has been intentionally placed for the sole purpose of emitting radio waves for harvesting [14] or from a source that is in place mainly to provide some other service, e.g. wireless Internet connections or telecommunications [3].

The selection of the harvesting frequency constrains the rest of the system design. The harvester antenna needs to have a resonant frequency equal to the frequency of interest. The output from the antenna also needs to be rectified to be usable by wireless sensors which means that the antenna needs to be impedance-matched to the rectifier for the low power levels to be efficiently transmitted between them. This matching reduces the effects of higher-order harmonics [3].

At the circuit level, RF energy-harvesting is modeled by an antenna, an impedance-matching network, a rectifier and a storage element such as a capacitor. In most cases, maximum power point tracking (MPPT) circuitry is included to keep the load conditions optimal for maximised power output. By regulating the output voltage or the output current, a point at which the power output is at a maximum can be found [15].

An example of a RF energy-harvesting setup can be seen in Fig. 6.

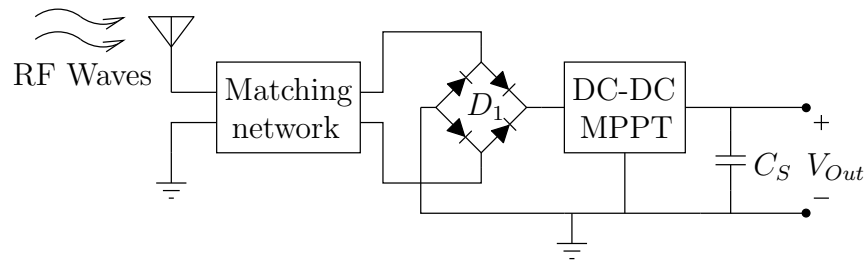


Figure 6: Radio-frequency energy-harvesting circuit

3 Theory - Circuit Elements

In this chapter, the circuit elements that constitute the system are introduced and explained. Current mirrors are covered first, because they were used in the designed system in an attempt to lower the minimum input voltage requirements. The variable active loads voltage-to-current-conversion is performed by trans-conductance amplifiers which are covered subsequently. Finally, a short description of analog-to-digital, and digital-to-analog conversion theory is made, as both are performed by the hardware.

3.1 Current Mirrors

A current mirror is an active circuit that, given a certain reference input current into the reference path, will keep the current through another path approximately the same, independent of the load voltage applied there. In essence the reference current is 'copied'. A basic current mirror consists of two matched transistors and it is essential that those are well matched for the circuit to precisely match the output current to the input current as explained below. A basic current mirror circuit with MOSFET transistors can be seen in Fig. 7.

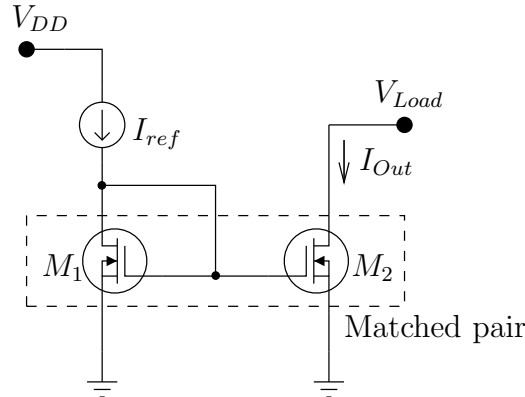


Figure 7: Current mirror circuit diagram (reproduced from [16])

The current that flows through transistor M_1 when it is in saturation is, according to [16],

$$I_{DS} = \frac{W}{2L} k' (V_{GS} - V_T)^2 (1 + \lambda V_{DS}), \quad (1)$$

where V_{GS} is the voltage difference between the gate and source terminals on the transistor, $V_{DS} = V_{DG} + V_{GS}$ is the voltage difference between the drain and source terminals, V_T is the transistor's threshold voltage, k' is the process transconductance parameter, λ is the channel-length modulation parameter and W and L are the transistor's width and length, respectively.

Since the gate of M_1 is connected to its drain, $V_{DG1} = 0$ and V_{DS1} is reduced to V_{GS1} . Therefore, V_{GS1} can be set by setting the value of I_{ref} . As a result, given that V_{Load} is sufficiently high to keep M_2 in saturation, I_{Load} will be equal to I_{ref} since $V_{GS2} = V_{GS1}$.

The reason for using matched pairs in current mirror designs is that the current that flows through transistor M_2 is also described by equation 1 and for that current to match the current going through M_1 as closely as possible, the unit-specific parameters W , L , k' , V_T and λ should be as close to equal as possible for the two transistors.

3.2 Trans-conductance Amplifiers

A trans-conductance amplifier is an active circuit that converts a voltage at the input to a corresponding current at the output [17]. An example of such a circuit can be seen in Fig. 8.

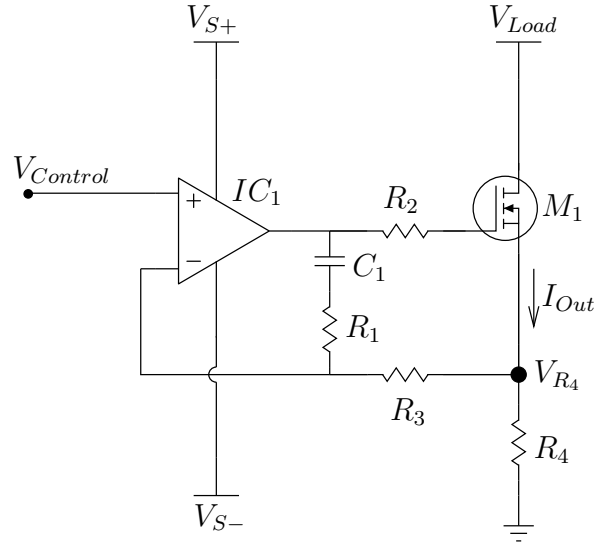


Figure 8: Trans-conductance amplifier circuit

Assuming an ideal op-amp with $V_+ = V_-$ and $I_{in+} = I_{in-} = 0$, IC_1 regulates V_{R4} to be equal to $V_{Control}$ since there is no current flowing through neither R_1 nor R_3 as by definition of the perfect operational amplifier. IC_1 will control the gate voltage of NMOS M_1 so that V_4 and $V_{control}$ become equal, a negative feedback mechanism. According to Ohm's law, I_{Out} can hence be determined as

$$I_{Out} = \frac{V_{Control}}{R_4} \quad (2)$$

The resistor R_2 is in place in practical designs to prevent parasitic oscillations

at the gate of M_1 , while C_1 and R_1 are compensation components to keep the design stable.

Errors in a amplifier circuit like this come primarily from characteristics of the operational amplifier chosen. Errors due to the finite open loop gain, input offset voltage and offset voltage drift will produce inaccuracies, but with careful selection of a operational amplifier they can be minimised below the requirements of the application [18].

3.3 Data Converters

A digital-to-analog converter (DAC) is a circuit that takes a digital number as an input (often as a bit-stream of a predefined number of bits through a serial connection) and outputs an analog voltage that corresponds to the digital number [19] [20].

It takes a continuous input voltage range $V_- - V_+$, a discrete numerical range of integers with 2^N elements, where N is the number of bits, and maps the input voltage range into the discrete range of numbers, so that voltage V_- corresponds to the lowest number in the range, and V_+ the highest number. The DAC can subsequently receive a digital number within the range, and output the voltage that corresponds to that number. This results in a finite set of allowed output voltages, where DACs with higher number of bits can support more discrete values and absolute accuracy, given the same dynamic voltage range [19].

Characteristics of DACs that need the designer's attention are the resolution needed, linearity, offset errors and bandwidth. The resolution, or number of bits along with the dynamic range decides the minimum voltage step size supported. Offset, gain and non-linearity (DNL/INL) errors are present in all DACs and need to be calibrated out if they are larger than the precision needed in the application, demonstrated graphically in Fig. 10, 9 and 11. Furthermore, the bandwidth and speed of a converter need to match the requirements for each application [21] [19] [20].

The relationship between dynamic range, bit resolution and voltage resolution is

$$V_{resolution} = \frac{\text{Dynamic Range}}{2^{bits}} \quad (3)$$

Figures graphically demonstrating errors in converters are shown next.

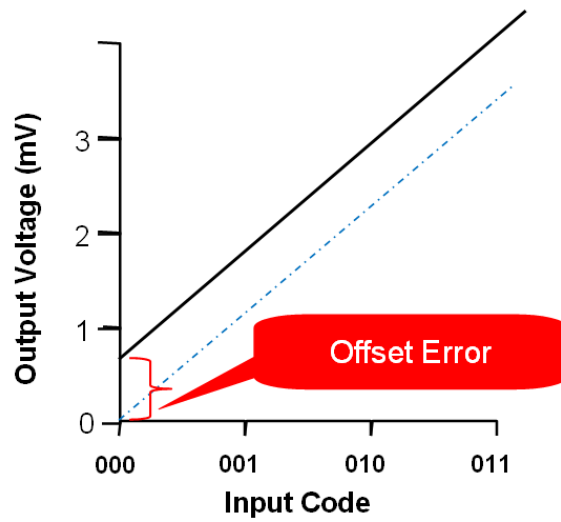


Figure 9: Offset Error Demonstrated (source:www.ti.com - Texas Instruments)

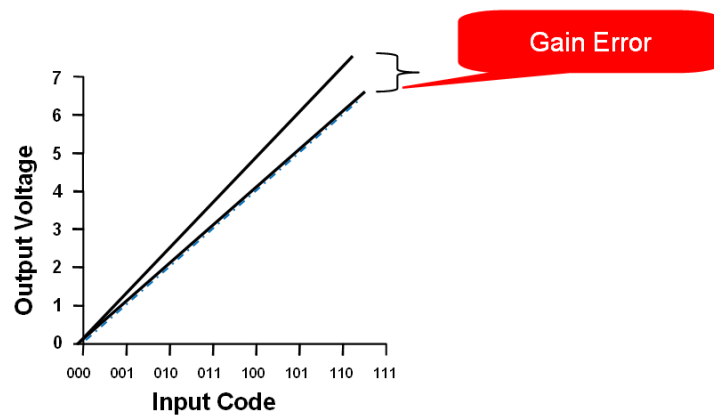


Figure 10: Gain Error Demonstrated (source:www.ti.com - Texas Instruments)

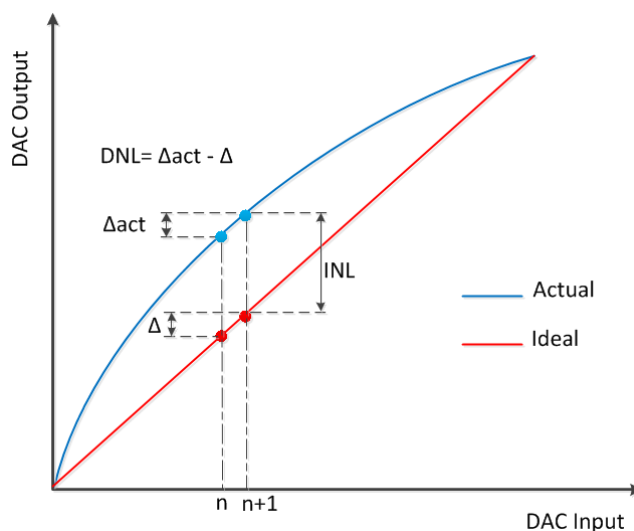


Figure 11: Nonlinearity Error Demonstrated (source:www.analog-eetimes.com)

An analog-to-digital converter (ADC), conversely to a DAC, is a circuit which takes an analog voltage signal as an input and outputs a digital number. The dynamic voltage range is the range the converter is capable of converting into a digital number. An ADC maps analog values into a digital number of N bits. So similar to the DAC it can only support a finite set of numerical values. Many of the same errors are present in ADCs as in DACs, namely offset, gain and non-linearity errors, which already have been demonstrated. The relationship between the dynamic range, bit resolution and voltage resolution is the same as for the DACs [21] [19] [22].

4 Pre-Study

To get preliminary knowledge and overview of the technology landscape, a pre-study was performed. The pre-study involved reading literature on state and progress of the energy-harvesting fields of interest. Also, included in the study, was a search for commercial applications and products involving energy-harvesting. As a result of the study, we were able to: 1) roughly estimate the viability of the various ways of energy-harvesting; 2) propose a method for evaluating systems based on them and 3) create a specification for a system based on the method, all in the context of powering wireless sensors. Covered below is the state of the art of the energy-harvesting methods of interest, how the specification was synthesized and finally an overview of the final specification.

4.1 Piezo-Electric Harvesting

Piezo-electric energy-harvesting is based on using materials that exhibit the piezo-electric effect. Piezo-electric materials deform when an electric field is applied to the material and conversely, produce potentials when physically deformed. This effect can be utilised to convert mechanical strain to electrical energy and back [13]. A more detailed theory on piezo-electricity was given in chapter 2.

4.1.1 Viability

Piezo-electric materials have proven to be viable sources of electrical energy [23], producing up to $625 \mu\text{W}/\text{cm}^3$ of energy into a capacitive load [13]. Energy densities of up to $330 \mu\text{W}/\text{cm}^3$ have been achieved by energy-harvesting systems that make use of piezo-electric materials [8]. Piezo-electric materials can be custom designed to fit specific applications. Attributes such as their open-circuit voltage and resonant frequency can be varied with material selection and geometry [13], making them suitable for engineering energy-harvesting products.

A disadvantage of piezo-electric materials is that they are resonant devices; they will only harvest efficiently when excited with frequencies close to their resonant frequency, i.e. they are inherently narrow-band devices. This property implies that piezo-electric harvesters need to be custom designed or tuned to match the excitation frequency of the environment they will reside in [13].

Piezo-electric materials are readily available commercially off-the-shelf today, and can be custom-made to fit energy-harvesting specific applications on demand. Examples of companies providing energy-harvesting products and services are Mide [24] and Piceramic [25].

4.2 Electro-Magnetic Harvesting

Electro-magnetic (EM) energy-harvesting is the use of moving magnets through magnetic coils such as transformers; it is a form of magnetic induction. Electro-

magnetic energy-harvesters based on moving magnets are of interest here because they can be used to harvest energy from vibrations.

4.2.1 Viability

Due to the presence of commercial applications utilising EM technology, it can be concluded that it is indeed viable. Electro-magnetic energy-harvesters have been commercialised and used successfully for wireless sensors in industrial applications. Prominent examples include the Swedish startup company Revibe Energy with their 'AMPG M₃' electro-magnetic vibrational harvester and Perpetuum's wirelessly monitored railway maintainance product.

Revibe's AMPG harvester sports an energy-harvesting capability of up to 280 mW at acceleration of over $3g$, with a frequency range of 5 – 100 Hz and a 5 – 15 Hz bandwidth. Their harvester is targeted towards industrial applications [26].

Perpetuum designed a wireless sensor that is mounted on the drivetrain of trains in the UK. The sensor estimates the state of the train tracks and state of the drivetrain ball bearings, correlating vibration to the state of the tracks and at the same time harvesting the energy from vibration to wirelessly power itself. It constantly uploads sensor data to a motherstation [27].

4.3 Radio-Frequency Harvesting

Radio-frequency (RF) energy-harvesting harvests energy from either intentional or unintentional radiation of electro-magnetic energy. In the case of energy-harvesting from sources that are in place to serve some other purpose than powering a harvester (GSM/Wifi), it is referred to as ambient energy-harvesting. RF energy-harvesting is of great interest when it comes to wireless sensors due to the capability of recharging sensors that are in otherwise unreachable places, such as inside solid concrete or enclosures. As the energy consumption of wireless sensors decreases, and the technology of RF energy-harvesting improves, the two edge closer to working reliably together, as further explored below.

4.4 Viability

RF-based harvesting has mostly existed in the research space for a very few years due to many technical challenges that need to be overcome. One of the main hindrances with RF harvesting is the RF-to-DC conversion efficiency, but one group managed to reach an efficiency of 60% at a free-space distance of 42 m by using specialised floating-gate transistors as rectifying diodes [28].

Until recently, ambient RF energy-harvesting has not been a competitive solution, compared to other methods, for powering wireless sensors due to low efficiency of such harvesting equipment. A recent study demonstrated that ambient harvesters can work at efficiencies of up to 40% in a semi-urban environment [3], i.e. levels which can compete with other energy-harvesting methods.

Efficiency levels when harvesting energy from dedicated sources that have been intentionally placed for the purpose of harvesting are considerably higher than in the ambient-harvesting case, or over 80 % [3].

Despite challenges in deploying and using RF-based harvesters, commercial solutions are available supporting RF harvesting designs. Powercast Corporation offers a complete solution that includes an RF-transmitter for intentional RF-harvesting at 850 – 950 MHz as well as receivers that convert the RF energy to DC voltage with conversion efficiencies of up to 70 % [14].

Furthermore, a commercial RF-based energy-harvester made by UK’s former science minister, Lord Drayson, called FreeVolt, made its debut recently. It is a device that harvests ambient RF energy and powers a personal air pollution sensor [29]. The technology is being further developed to trickle charge electronic devices and power general IoT devices [30].

As the efficiency of digital systems increases, RF energy-harvesting may be starting to become viable to power small devices and sensors. This appears to be the case considering the first ambient RF harvesting commercial products are starting to emerge.

4.5 Specification Synthesis

Here, an explanation of how a specification was synthesised for an energy-harvester test valuation system and the final targeted specification is offered. The capability aimed for is described closely and primary use cases are identified. The specification synthesis was performed entirely by the authors of this thesis essay, by looking at commercial examples and the technological details of the harvesting technologies of interest.

4.5.1 Use Cases

Primary use cases are motivated and presented here. When designing for energy-harvesting applications there are numerous experiments a designer might want to perform on materials and energy-harvesting systems, and interactions he/she might want to observe between the energy-harvesting and wireless sensor sub-systems. Furthermore, a user might want to use the system to validate a design. The use cases are identified in the following list:

- Use the system to find resonance frequency of energy-harvesters and piezo-electric material configurations. The resonance frequency of piezo-electric materials changes with mechanical parameters such as material length and load mass. EM energy-harvesters have a bandwidth limited frequency response and RF energy-harvesters have high frequency dependence as well. It is a critical design aspect to have the frequency correct as some harvesters such as piezo-electric and RF are quite narrow-band.
- Use the system to find the maximal power point of harvesters and piezo-electric material composites. Piezo-electric materials have a certain power output where they produce energy most efficiently. Finding this point may

be of interest to a designer so that the output voltage of the harvester can be set to spend as much time as possible around the maximal power point.

- Use the system in the field to find optimal orientations and placements for energy-harvesting configurations and products, observing the power that can be drawn under different circumstances.
- Use the system to emulate a wireless sensor and observe the interaction between the energy-harvesting and wireless sensor subsystems while deployed in the field for design or verification purposes. By observing the voltage output directly from the harvester and/or the status of the energy storage element, the user might identify the system's margin to failure, i.e. how far from non-operational voltage levels the output is. Insight into the long-term stability of the environment to excite the harvester could be estimated.

4.5.2 Proposed Capability

The proposed capability of a test system capable of evaluating energy-harvesting systems for wireless sensors, is the capability to evaluate harvesters being excited either in a controlled situation in a lab, or in the field. Therefore, the system needs to be mobile, i.e. easily transferable. It needs support for display, keyboard and mouse for operation with a graphical user interface (GUI) environment. A console version, to be operated remotely, may be supported later. For time budget reasons the test system should use open source and easy to use platforms, such as the Raspberry Pi [31] and programming languages that aid fast development time such as Python.

4.5.3 Sensor Emulation

The test system should be able to draw power according to a pre-defined profile, emulating a sensor. This can be done, for example with a X percent higher margin to verify that a harvesting system is capable of providing the power needed over time while drawing current the system samples the output voltage of the harvesting system to calculate total power drawn. It would be an exciting prospect to be able to expedite validation experiments and sensor power profile emulations. It is evident, however, that the interest in evaluating sensors is in the context of doing so in the final environment, at the real energy input. Expediting the environmental process to shorter timescales may not be feasible under all circumstances, e.g., when increasing the power input and increasing proportionally the frequency behaviour. This means that a sensor emulation is likely done in real time which may involve long-term measurements. Exceptions to this may be special circumstances where the environment can be modified to emulate faster passing of time. Therefore, the system needs to be able to support long-term data acquisition.

4.5.4 System Characterisation

The system should be able to record the voltage, as current is swept, to find the maximum power point or sourcing capability under a given excitation. With a storage extension, such as the capability to install for example a supercapacitor across the inputs, it should be able to record how the system behaves when charging such a supercapacitor or alternatively a battery-based storage design.

4.5.5 Material Characterisation

The system, with the rectifier extension, should be able to characterise piezo-electric materials by finding the maximum power point. This can be done based on the output voltage of the harvester and the value of the controlled current drawn out of the system.

4.5.6 Maximum Input Voltage

Raw outputs from piezo-electric materials can range from a few Volts up to hundreds. Electro-magnetic harvesting systems tend to produce low (< 100 mV) voltages but high currents. RF harvesting systems produce low voltages at the rectifier output but are rarely used without specialised rectifiers and built in circuitry for maximum power point tracking and up-conversion into a storage unit. RF harvesters will thus always be evaluated as complete harvesters. Complete harvesters are harvesters with maximum power point tracking and DC-DC conversion from a rectifier into a storage element included. Complete harvesters for wireless sensors are typically designed to charge and regulate a supercapacitor to a low system voltage of 1.2 – 5.5 V. The reason for that voltage range is likely both to generate standard system voltages and to generate comfortable voltages that can be down-converted again by nano-power regulators, in the arrangement when MCU sub-system voltages are being minimised and the storage element voltage maximised. These nano-power converters typically allow only a limited input voltage range.

The maximum power point for piezo-electric materials is usually positioned at approximately half the open-circuit voltage for a given excitation level. Based on that, it is only when directly evaluating high voltage piezo-electric materials without built in power point tracking and DC-DC conversion, that high voltages are seen at the input. In that case, a storage capacitor is still used to capture the energy from a rectifier and this capacitor can be sized to limit the voltage after the rectifier. The capacitor reduces the voltage seen unless it is allowed to charge up without limits to the open-circuit voltage of the piezo-electric material.

In practise, with knowledge of the environment they operate in, materials can be designed to generate comfortable open-circuit voltages to be harvested. As supercapacitors generally have low voltage tolerances as seen in commercial offerings, harvesting systems for wireless sensors will be designed to operate with open-circuit voltages in the 5 – 20 V range, placing the maximum power point at 2.5 – 10 V.

With all things considered, a support for voltages up to approximately 10 V should suffice to evaluate complete harvesters, that is those with built in power point tracking and conversion. Most piezo-electric materials intended for wireless sensor applications will also be covered within that range.

4.5.7 Minimum Input Voltage

The minimum voltage supported by the load cell should be low enough to accurately evaluate the capability of complete harvesters to keep up against controlled power consumption. The lowest operating point of low power sensor circuitry to function, in the 1.2 V range, is a potential prospect. But in practise there may be interest in tracking temporary dips into regions of non-availability. So with that in mind the lower the better.

Electro-magnetic harvesters without conditioning circuitry provide low (< 100 mV) voltages, too low to even rectify with traditional diodes. In practice, a step-up-transformer is used to gain higher voltages. It is assumed a step-up-transformer and a rectifying bridge are present when these are evaluated. This means that the low-voltage-output of electro-magnetic harvesters do not impose a particular restriction on the minimum voltage level that needs to be supported by the system.

For evaluation of piezo-electric materials, the minimum voltage is not of great concern since they are 'high voltage' generators. The minimum voltage is more important when harvesting small vibrational forces so the lower minimum voltage the better presumably.

RF harvesting is assumed to always come in a 'complete' form due to the special design constraints of the rectifier and maximum power point tracking. Based on the points above, a reasonable minimum input voltage to aim for is on the order of 50 – 100 mV.

4.5.8 Minimum Current

Wireless sensor MCUs in deep sleep mode can draw extremely low currents, in the order of hundreds of nano-amperes. It may be difficult to accurately control currents from low hundreds of nano-amperes to milli-amperes. However, in practice, wireless sensor power consumption is dominated by their on-time, the active duty cycle, meaning that average currents can emulate them to a large extent. The average current in majority of applications will always be larger than the sleep current by a large margin, meaning that current capability in the couple of hundred nano-Amperes or even single micro-Amperes will suffice in most applications. Setting the lower bound at $1 \mu\text{A}$ is reasonable.

4.5.9 Maximum Current

Piezo-electric and RF harvesters are low current devices while electro-magnetic ones are high current. Wireless sensors by design draw low power levels, which in practical designs when drawing power from energy storage with voltages in

the range of 1.8 – 5 V results in low currents. Ultra low power MCUs in active mode may draw typically 5 – 15 mA. The most current demanding use case is evaluating the maximum power capability of harvesters. Commercial examples can be found for a electro-magnetic harvester capable of 280 mW power levels under best case conditions [26]. At a 1.2V output voltage this implies a current capability of 250 mA. This would be more than plenty for most applications, considering that a modern active-mode wireless-sensor MCU, such as the CC2640 from Texas Instruments [6], can run on as little as 50 mW at 100 % duty cycle.

4.5.10 Power

Based on the voltage and current requirements, the load cell needs to support power levels from a few hundred nW up to approximately 300 mW.

4.5.11 Leakage

Leakage currents may affect long-term accuracy of measurements when emulating a wireless sensor and must be substantially less than average currents. Basing the leakage current on the minimum current capability of the load cell, it would seem reasonable to set the leakage current as some fraction of that. At 10 % the leakage requirement is 100 nA.

4.5.12 Accuracy

Absolute error of maximum 5 % at the lowest current supported and average relative error of 1 % should suffice for most evaluation purposes. A 50 nA error at the lowest step will have negligible effect on any measurement as average currents are much higher and a relative average error of 1 % should satisfy likewise as applications in reality would never run with a 1 % margin from minimum average operating power capability from the power source.

4.5.13 Bandwidth and Response Time

The function of emulating sensors will set the maximum bandwidth and response time required for the design. A wireless sensor may have an active mode duty cycle down in the tens of milliseconds. If the intention is to emulate sensors accurately over time, then supporting a duty cycle of 1 % or 10 ms is a conservative choice between capability of the test system and difficulty with the design. Being able to emulate 10 ms spur of activity, would call for response times of maximum 100 μ s for 1 % accuracy. The corresponding bandwidth is approximately 3.5 kHz.

4.6 Final Specification

The summary of design requirements for the active load current control, and the data acquisition for the system is listed in Tables 1, 2 and 3 below. Some

parameters have been budgeted between the two, such as the total leakage current which can be found in both tables.

Table 1: Platform requirements

Requirement Type	Type	Requirement
Platform	Hardware	Raspberry Pi
Platform	OS	Linux
Platform	Application Software	Python

Table 2: Analog-to-digital conversion

Requirement	Min	Max
Input Voltage	0.1 V	10 V
Leakage Current	N/A	50 nA
Average Relative Error	5 %	N/A
Rise Time	N/A	1 ms

Table 3: Active load

Requirement	Min	Max
Input Voltage	0.05 V	10 V
Input Current	1 μ A	250 mA
Smallest Current Step	1 μ A	N/A
Power Dissipation	N/A	280 mW
Leakage Current	N/A	50 nA
Absolute Error @ Smallest Current Step	N/A	5 %
Average Relative Error	N/A	1 %
Rise Time	N/A	100 μ s
Bandwidth	DC	3.5 kHz

5 System Design and Validation Method

In this chapter, the system design is presented. The system, which has been given the name 'Athol', consists of hardware and control software. Both parts are explained in detail below, that includes how they are implemented and how verification of their functionality is performed.

5.1 Implementation

The following sections cover the implementation details for the Athol hardware and software.

5.1.1 Hardware: Overview

Presented in Fig. 12 is an overview of the Athol hardware system.

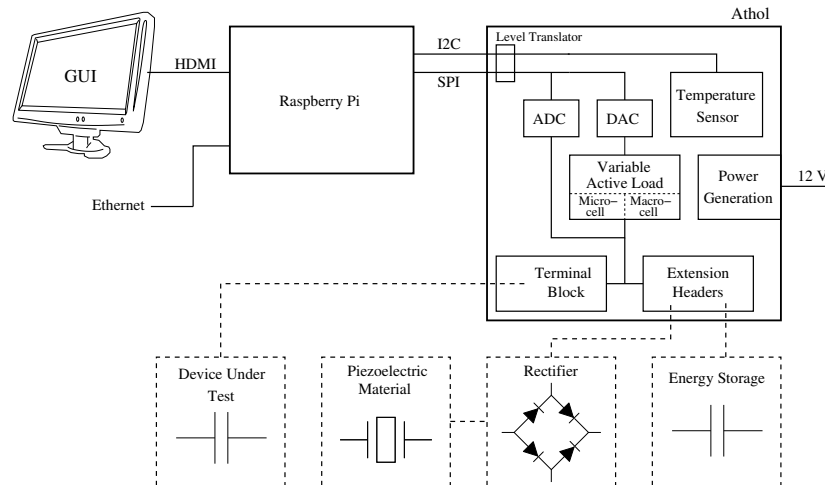


Figure 12: Overview of Athol System and its Environment

Creating a test platform with all the required functionality from scratch, and providing a reasonable HMI (Human Machine Interface) interaction is time-consuming and difficult. However, by utilising the Raspberry Pi open-source platform, it was easy to quickly get features such as display connectivity, mouse and keyboard functionality to make up a complete evaluation and test instrument within the time budget of the project. The Raspberry Pi platform brings network connectivity and a familiar Linux working environment, with dynamic time-saving languages such as Python to users of the platform. The Raspberry Pi foundation provides a standard called HAT (Hardware Attached on Top), which when fulfilled guarantees future compatibility with the Raspberry Pi platform with new releases. Athol fulfills that standard. The Athol hardware for the project is mounted on top of the raspberry Pi, to the Raspberry

Pi GPIO 40-pin header. Level translation between 3.3 V and 5 V takes place by level translation circuitry between the Raspberry Pi and the Athol hardware. These platform choices turned out to be a good decision and reduced the time investment needed in the project substantially.

The high-level function of the system is that the GUI on the Raspberry Pi, connected to a display, mouse and keyboard, is used to give commands to the hardware, which in turn draws variable constant current or constant power from a piezo-electric material or another device under test. There are two kinds of external input connections: one is a terminal block connector for the device under test, others are headers to allow external extensions, in the form of small PCBs or wires to be connected across the input. The extensions could be a supercapacitor, a rectifying bridge for piezo-electric materials or circuitry to recharge a battery, mimicking the power architecture and dynamics of various wireless systems.

A core feature of the measurement system is the variable active load, which due to its six decade current range consists of two separate active loads with varying accuracy. The more accurate one, referred to from here on as the 'micro-cell', is capable of drawing currents from 0 mA to 10 mA. The other one, the 'macro-cell', was designed to cover currents from 10 mA to 250 mA. They are switched as needed by the software to cover a combined current range from 0 to 250 mA.

The micro-cell can support, albeit with tradeoff against the dynamic current range, individual current steps as small and likely even smaller than 100 nA.

The current steps are controlled by the DAC, which outputs a control voltage into the load-cells. An ADC measures the input voltage to the system. Combined with the board connections, these modules form a test and measurement system that can draw controlled currents and power levels as suited in order to evaluate energy-harvesting systems, while still being very small and portable in nature and thus applicable for in-field deployment and evaluation.

5.1.2 Hardware: ADC

The analog-to-digital conversion sub-circuit is shown in Fig. 13.

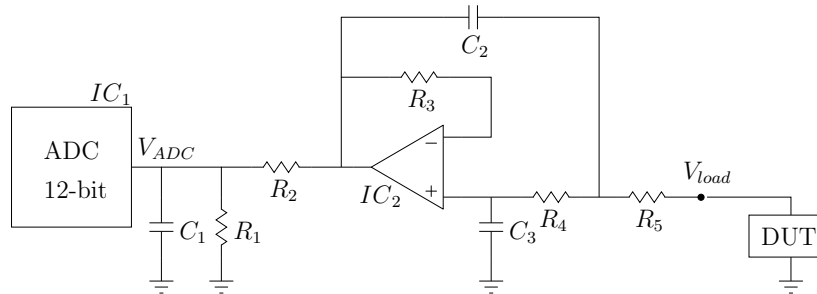


Figure 13: Analog-to-digital conversion as it is implemented in Athol

The important aspects that needed consideration when the circuit was designed was that the total leakage at the input cannot exceed 100 nA, the input voltage range is larger than typical input voltage ranges of chip ADCs, the input impedance into the ADC input needs to be controlled and an anti-aliasing filter is needed before the ADC input.

The circuit shown in Fig. 13 consists of an operational amplifier forming a very high input impedance buffer amplifier, along with a resistor divider to scale the input voltage range. The operational amplifier selected was the LMC6041 [32] (IC_2), with input bias currents in the femto-Ampere range, tolerant with respect to latchups, single supply, and a large common-mode voltage range that includes ground. A two-pole Sallen-Key filter can be formed by proper choice of passive components C_2 , C_3 , R_3 , R_4 , R_5 . An additional pole can be formed out of the resistor divider R_1 , R_2 that scales the op-amp output before the ADC by proper selection of the value for C_1 . The selected ADC, MPC3201 [33] (IC_1), has a resolution of 12 bits and a 0 – 5 V dynamic input voltage range, calling for a resistor divider ratio of 1 : 2.

While appendix A contains the detailed design calculations, some notable characteristics for the design are a voltage resolution of approximately 0.2 mV, noise density and SNR which amounts to 136 dB considering intrinsic noise of the OPA277 [34] (IC_2), offset error due to the operational amplifier which amounts to a 18.35 dB resolution. Overall, with calibration, close to the full 12-bit effective SNR should be realised as errors are much smaller than the value corresponding to a least significant bit.

The ADC IC itself, MPC3201, was chosen due to its simplicity on the SPI communication side. Sample conversion takes place as data is clocked out on the SPI bus, meaning that a single read triggers and results in the acquisition of a sample.

5.1.3 Hardware: DAC

The digital-to-analog conversion schematic, where the control voltage for the load cells is generated is shown in Fig. 14.

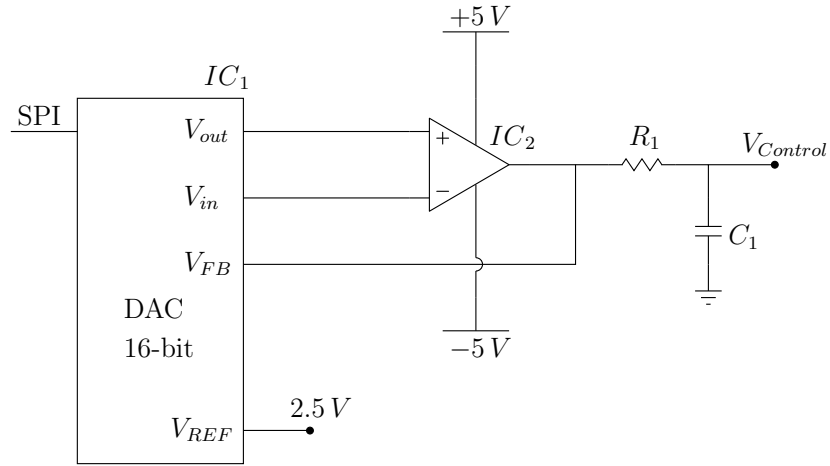


Figure 14: Digital-to-analog conversion as it is implemented in Athol

The DAC itself, the 16-bit DAC8824 (IC_1), along with the operational amplifier OPA277 (IC_2) forms a bipolar digital-to-analog conversion system that outputs an analog voltage of $\pm 2.5\text{ V}$. Only the positive range of the DAC is actually used, sacrificing half the range. In return, the circuit behaves well around zero output voltage, where many single ended digital-to-analog converters have issues reaching ground potential. On startup, the DAC will set its output voltage at the middle of its dynamic output range, which is 0 V for bipolar operation. The DAC was chosen due to its simple SPI operation; a write is all that is needed to change the output.

The DAC has offset and gain errors but those can be calibrated out at the software level and the bipolar configuration helps to calibrate the zero level if the offset turns on the load cells prematurely.

5.1.4 Hardware: micro-cell

The micro-cell, which in essence is a relatively basic trans-impedance amplifier, followed by current mirrors, is shown in Fig. 15.

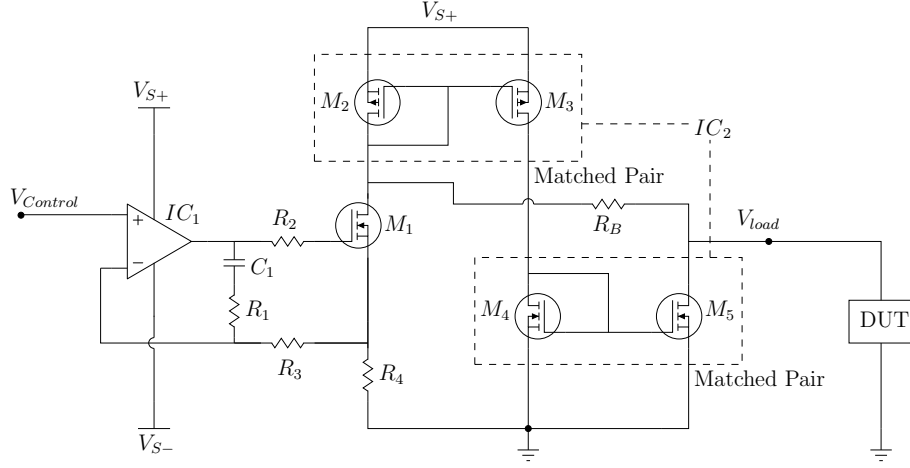


Figure 15: Micro-cell, intended for drawing currents in the range 0 – 10 mA

The circuit shown draws current in accordance to the control voltage V_{load} applied. The control voltage, $V_{Control}$, appears directly over the current setting resistor R_4 due to the unity gain configuration and feedback. Due to the open-loop nature of the design, it needs to be very stable against temperature changes to fulfill the specification. For that reason the operational amplifier IC_1 is the LTC2051 [35], which is a special type of operational amplifier called a chopper-amplifier, or auto-zero amplifier, which features very low offset voltage errors and offset drift over temperature. This ultimately results in a very temperature-stable design, drawing precise current $\frac{V_{load}}{R_4}$ through MOSFET M_1 .

If the current mirrors, formed by $M_2 - M_5$ (in one IC, IC_2) are removed, and the V_{load} voltage is directly connected to the drain of M_1 through bypass resistor R_b , then the input voltage range will be limited by the voltage over $R_4 + V_{DS}$ required to properly set the current through the cell. Because the drain of M_5 in the final low-side current mirror can in theory approach 0 V, the voltage dependence on the output of the load cell trans-impedance amplifier can be transformed into practically 0 V. However, this relies on the mirror MOSFETs being very well matched on a chip level and being capable of accurately copying the current generated by the trans-impedance amplifier twice. The ability to copy the current accurately enough was not assured, and hence a bypass mechanism was designed where a 0Ω resistor R_b could bypass the mirror, so that it could be removed if needed, trading off the minimum voltage input requirements for higher accuracy. Error and noise contribution were calculated to be within range of the specification, see appendix A for further detail and calculations for the micro-cell.

5.1.5 Hardware: macro-cell

The macro-cell, which is also a transimpedance amplifier, is shown here in Fig. 16.

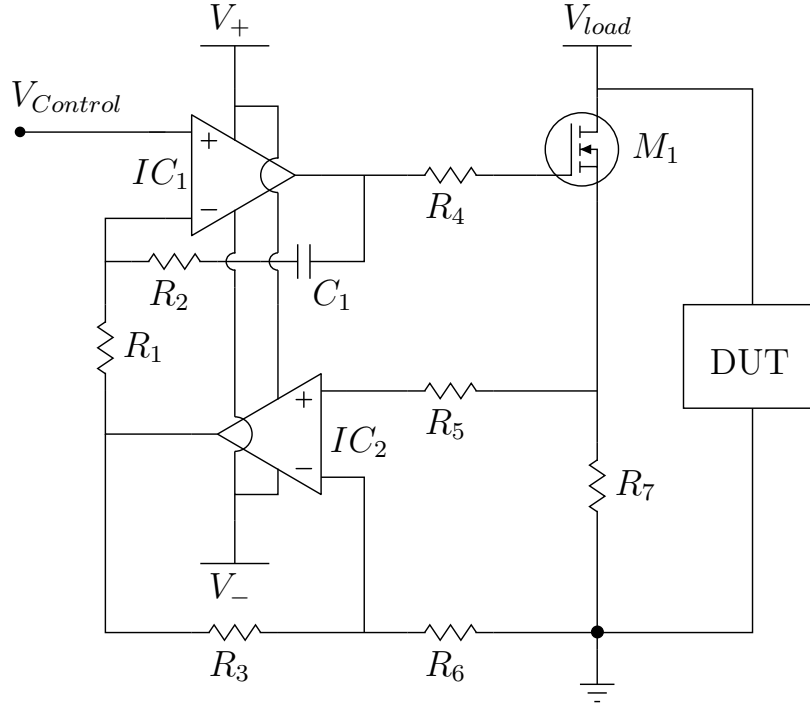


Figure 16: Macro-cell, intended for drawing currents in the range 10 – 250 mA

The macro-cell covers the upper part of the current dynamic range. It has a similar topology, except that additional feedback gain is generated by IC_2 in the overall feedback path to decrease the voltage that appears over R_7 , as the macro-cell has no current mirror to transform the input voltage requirements. A gain of 10 was used which means that when the control voltage is at a full scale of 2.5 V the voltage over R_7 is only 0.25 V. The additional operational amplifier in the feedback-path increases static errors due to offset voltages and for that reason, the macro-cell is not suitable for very low currents. The feedback path gain is set by R_3 and R_6 . Compensation components R_1 , R_2 , C_1 and R_4 are needed to stabilise and control the response of the circuit.

As this is an open-loop design, chopper amplifiers were used to get good temperature and drift characteristics, eliminating the need for closing the loop. The chopper amplifier selected was the LTC2051 [35], which has good tradeoff between performance and price.

Error and noise contribution were calculated to be within range of the specification, see appendix A for further detail and calculations for the macro-cell.

5.1.6 Software: Overview and Architecture

We wrote the control software for Athol in the Python [36] programming language. This language was chosen for two reasons; firstly because we are familiar and comfortable with developing software using it and secondly because it is dynamically typed and interpreted, which we find makes development more convenient and faster than with statically typed languages.

A GUI was programmed using PySide [37], Python bindings for the GUI toolkit Qt [38], primarily because the documentation for the bindings is very extensive and they are simple to use. The architecture of the software is an adaptation of the model-view-controller (MVC) application structure paradigm [39].

An overview of the software architecture can be seen in Fig. 17.

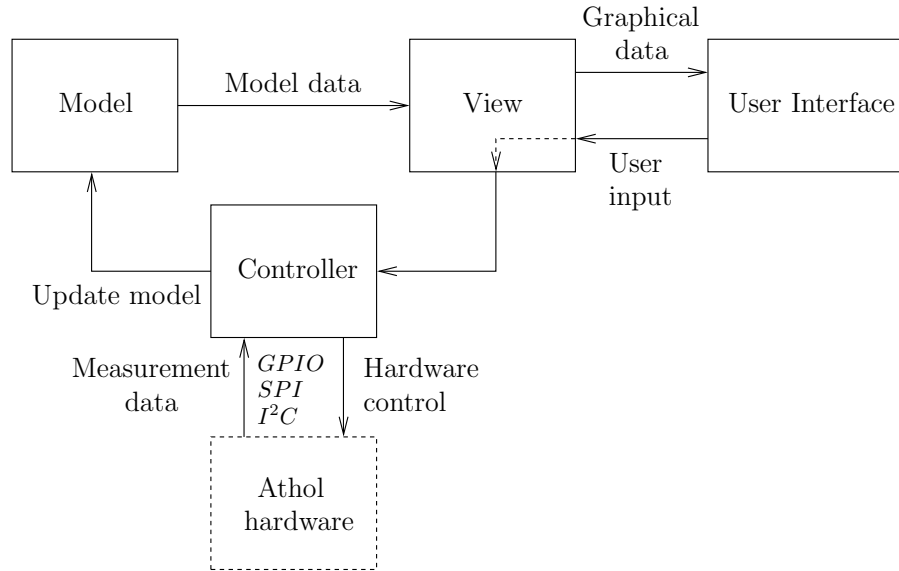


Figure 17: Overview of the Athol software architecture

The model holds the data of the Athol software, e.g. data that determines how a certain wireless sensor should be emulated or the state of an ongoing emulation. The view is responsible for sending data from the model to the user interface for display as well as for receiving input from the user and relaying it to the controller. The controller receives data from the view, performs any calculations involving that data if necessary and updates the model. The controller also communicates with the Athol hardware via serial peripheral interface (SPI), inter-integrated circuit (I²C) and general-purpose input/output (GPIO) communication protocols to send control signals and to read measurement data such as board temperature and input voltage level.

It became clear in the pre-study stage that the Python modules for connecting to the Athol hardware would possibly not be fast enough to meet the

system requirements since they run in the user space of the Linux operating system which is not designed to provide real-time functionality. The scheduler of the operating system could therefore interrupt the software, resulting in jitter in the timing of the communication signals.

One way of improving the communication reliability would be to write a kernel driver that would handle the communications between the Raspberry Pi and the Athol hardware by reading data from the board and writing it to a memory buffer that the Python software could access. A decision was taken to avoid this complication until the Python communication modules had proven themselves to be inadequate since it would increase the complexity of the software significantly.

5.1.7 Software: Functionality

The purpose of the Athol software is to make it possible for the user to have the Athol hardware draw current from the device under test in various ways. We decided to implement three input methods for the user and they are called emulate, manual and sweep.

In the emulate mode, the user supplies a file of comma-separated current values and a sample rate. The file is parsed by the program and the hardware is commanded to draw current equal the desired values at the given sample rate. The manual mode accepts a sample rate and one of two possible inputs, desired current or desired power. The program then commands the hardware to either draw constant current equal to the desired current value or the current needed for the instantaneous power to match the desired power value. The sweep mode has four parameters which are minimum current, maximum current, duration and step size. The program calculates a list of current values that match those parameters and feeds the values to the hardware, one by one, at time intervals that are calculated from the duration and step size values.

There is a limit of how much current the Athol hardware can draw from a system under test, as explained earlier in this chapter. Therefore, the Athol software monitors the input voltage from the device under test and commands the hardware to draw current that is as close to the desired value as possible that the device under test can supply.

The Athol GUI is shown in Fig. 18. The three aforementioned modes can be selected using the tabs in the upper left corner.

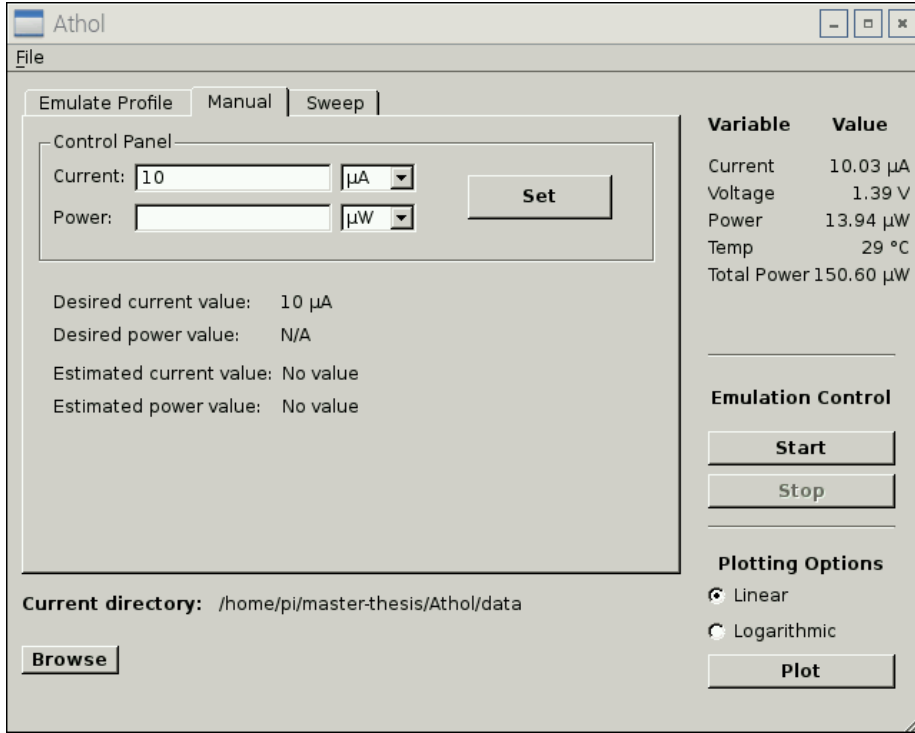


Figure 18: The Athol graphical user interface

After the user has performed a test, plots containing measurement results can be shown by the push of a button. The plots are made using the Python plotting library Matplotlib [40] and an example of a plot made by the Athol software is shown in chapter 6. The measurement data is also logged and saved to a file automatically.

The Athol software calculates the approximate power that has been drawn from a system under test. This is accomplished by performing integration on instantaneous power values that are obtained by multiplying the current that is being drawn from the system under test by its input voltage. The integration is done using the trapezoidal rule [41],

$$\int_a^b P(t)dt \approx (b-a)\frac{P(b)+P(a)}{2}, \quad (4)$$

where $P(t)$ is the instantaneous power value at time t and a and b are two points in time. The system performs one such calculation for each sample obtained and the sum of those calculations is an approximation of the total power drained from the system. The sampling rate of the system is fully configurable by the user.

5.2 Validation Method

The validation strategy for the measurement results of the thesis was to build more than one instance of the Athol hardware, making the same or similar measurements on them, and comparing them together where possible. This procedure increased the significance of the results, and likelihood that they are not just a lucky combination of component variances.

Effort was put into using and documenting test equipment used while gathering results and the circumstances present. Proper, calibrated instruments were used and where applicable, doubts of insufficient accuracy are clearly stated.

By using precision instruments, Athol could be validated to be functionally correct and within stated capability, but it was harder to do so towards the capability of the complete system to evaluate energy-harvesting systems, which is based on personal experience and insight, and could take a long time to fully materialise until an assortment of different energy-harvesting systems have been evaluated. Athol has however been used to evaluate real piezo-electric materials that harvest energy from vibrations, by the authors. The Athol test system was calibrated with a GWINSTEK GDM-8341 5-1/2 digit multimeter [42] bench-top instrument, with a resolution of 10 nA at the lowest current range before experiments were performed.

6 Results

In the following sections, test system performance results and data on its ability to evaluate an energy-harvesting system are presented.

6.1 ADC

Results from the analog-to-digital conversion module of the system are presented here. The test setup was the Athol hardware mated to the Raspberry Pi and powered from the 12 V wall wart-power input. The tools used were GWINSTEK GDM-8341 5-1/2 digit multimeter [42] and a Aim-TTI PL303QMD quad-mode dual channel power supply with configurable output voltages [43]. The multimeter was used to measure and manually configure the power supply output voltage to apply a known voltage to the input of the Athol measurement system. This way the transfer function of the ADC was evaluated. Measurements were made for two different boards with identical setups.

Board 1 yielded the result shown in Fig. 19. It shows the expected and measured outputs, relative error and absolute offset error. Relative error is the percentage error of measured to expected, and the absolute offset error is the real value subtracted from the expected one.

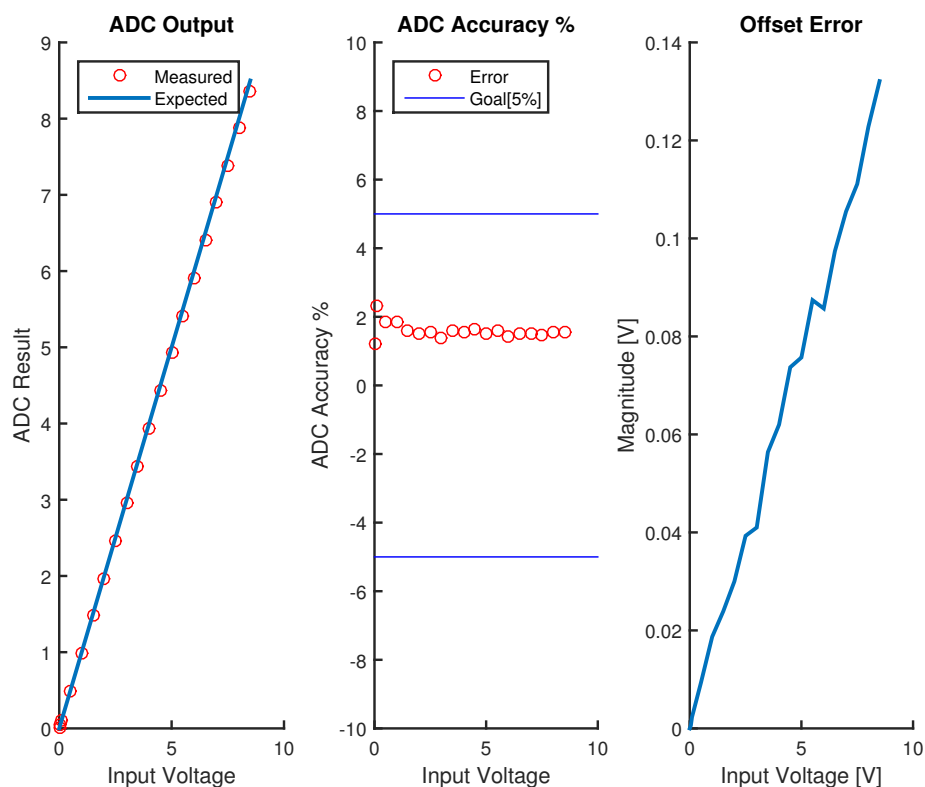


Figure 19: Results from the analog-to-digital conversion in board 1.

It is evident from the measurement data that the expected and measured outputs agree very well. The relative accuracy is within the 5% target bounds for all measured values and hence conforms to the specification. The mean relative error is 1.58%. The main error components are the combined gain errors introduced by the ADC, the resistor divider and the operational amplifier, and the offset error contributed by the ADC and the operational amplifier. The linearly sloping absolute offset error seen is the primary hallmark of a gain error, which can be calibrated out in the digital domain.

Board 2 yielded the the result shown in Fig. 20, showing the expected and measured output, relative error and absolute offset error like before.

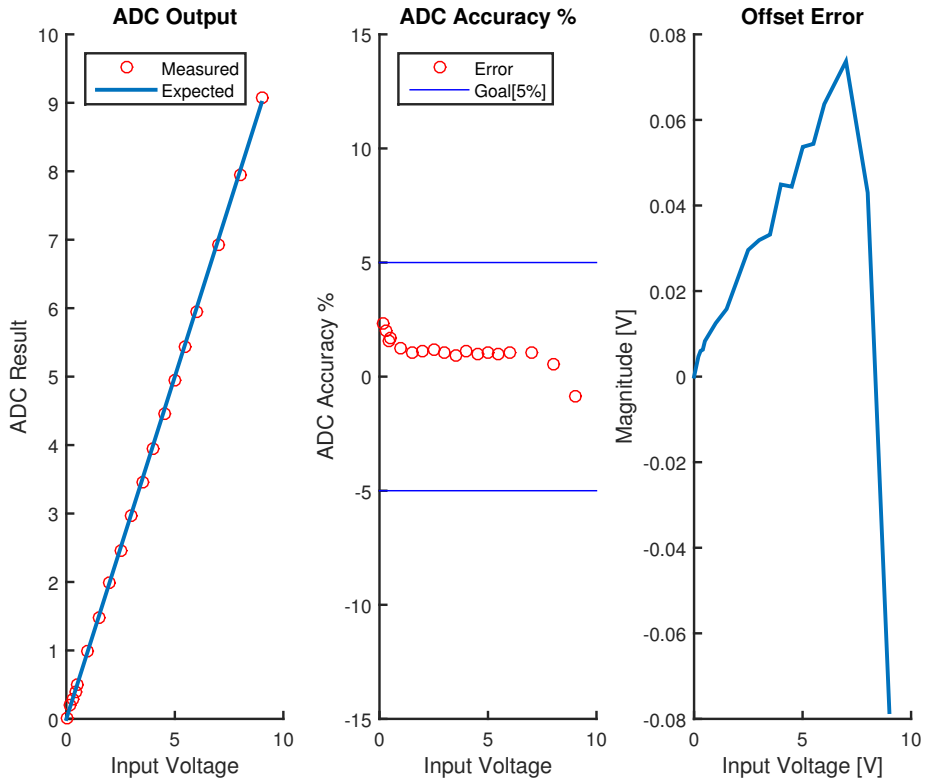


Figure 20: Results from the analog-to-digital conversion in board 2.

The results are very similar to the ones for board 1, except this one was measured up to 9 V instead of stopping at 8.5 V where we hit the common mode input voltage range limit of the operational-amplifier, resulting in the sudden change downwards jump in the absolute error at the end of the dynamic range. Because exceeding the common mode voltage range can result in a latchup, the usable dynamic input voltage range does not fulfill the specification entirely.

6.2 Macro-Cell

The macro-cell was measured by utilising the GWINSTEK GDM-8341 5-1/2 digit bench-top multimeter in current measurement mode and a PL303QMD lab power supply applying 2V to the input of the Athol system. The current path was routed through the bench-top multimeter.

Fig. 21 presents the result from sweeping the current of the macro-cell on board 1, showing the expected and measured output, relative error and absolute offset error.

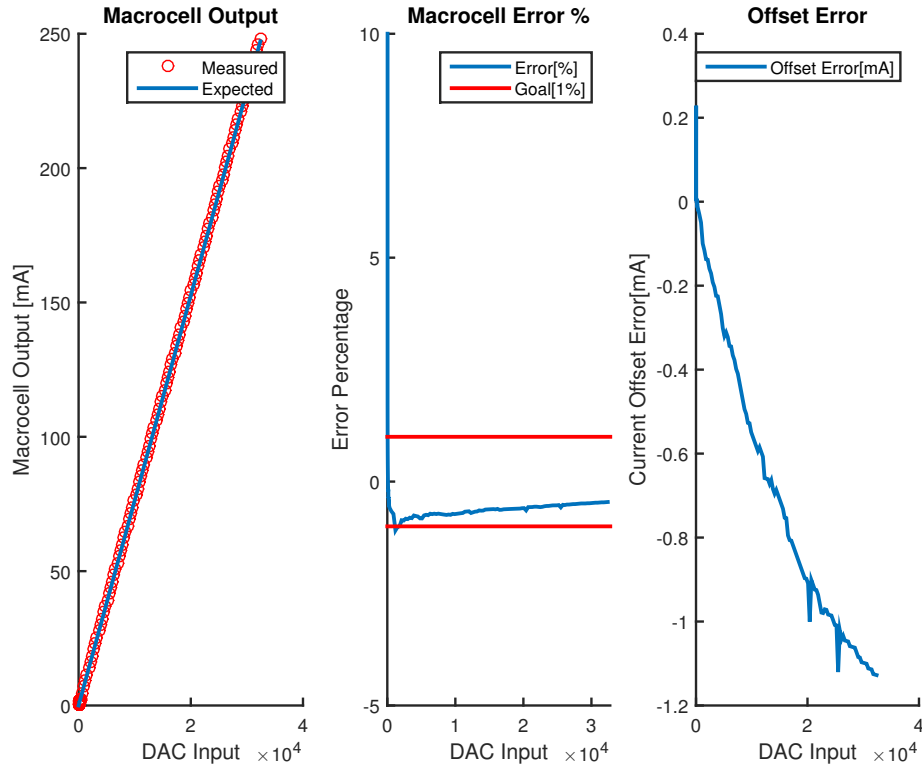


Figure 21: Macro-cell on board 1

The transfer function for the cell looks good. However, it does not turn on until at approximately count 40, where it outputs $300 \mu A$. Increased offset contributions from the extra operational-amplifier and feedback loop gain may be causing this effect. It is of no consequence however as it was not intended to be used at these low currents. Shortly after it has recovered, the cell dips slightly out of the error bounds, but otherwise it stays inside the error bounds for the rest of the dynamic range. The offset error is for the most part linearly sloping, but appears to have a small non-linear factor as well.

Fig. 21 shows the result from sweeping the current of the macro-cell on board 2. It shows the expected and measured output, relative error and absolute offset error.

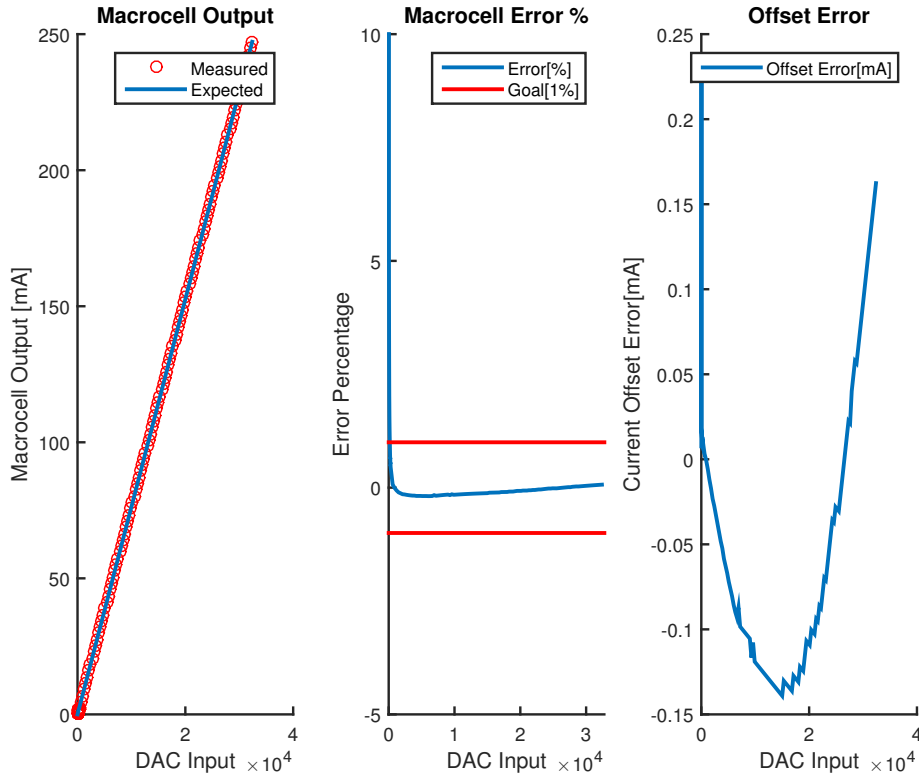


Figure 22: Macro-cell on board 2

This cell, like the one on board 1, seems to have a decent looking transfer function. It also turns on at approximately count 40, jumping up to $300 \mu\text{A}$. It stays within error bounds for the entire dynamic range. The primary difference between the results from the cell on board 1 is that the offset error has a significantly stronger non-linear effect. It has the same slope as well. The source of this error is not known, but it may be related to variances in the characteristics of the chopper amplifiers used.

6.3 Micro-Cell With Mirror

Results from the micro-cell are presented here. The micro cell was measured by utilising GWINSTEK GDM-8341 5-1/2 digit benchtop multimeter in current measurement mode and a lab power supply PL303QMD applying 2V to the input of the Athol system, routed through the bench-top multimeter. Our first measurements were with an additional multimeter measuring the output voltage of the power supply, but that configuration caused leakage currents that affected the measurements significantly at the lowest current levels.

Fig. 23 shows the measured results when the current mirror was in place for

the micro-cell in board 1. The expected and measured output currents, relative percentage error between them, and the absolute difference are shown.

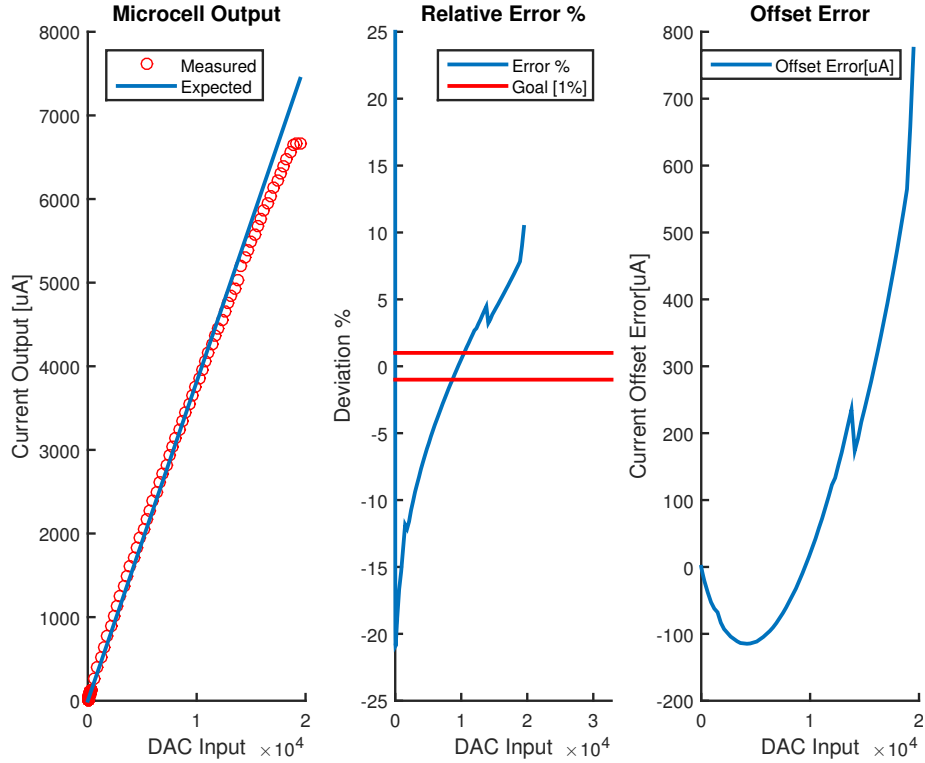


Figure 23: Micro-cell with mirror on board 1

It is evident from Fig. 23 that we have strong effects from non-linear errors. The error is outside the error bounds as well for a greater majority of the dynamic range so this configuration does not fulfill the specification. The error is very high in the beginning for the initial values, but quickly stabilises to about -20% but slopes non-linearly to approximately $+15\%$ over the dynamic range before the mirrors saturate at 6.3 mA , where it starts increasing quickly. A strong saturation effect is seen around 6.5 mA where the mirrors cannot pass more current, far from the desired 10 mA range.

Sharp corners artifacts can be seen in the figure, resembling discontinuities. These artifacts are the result of the benchtop multimeter switching between measurement ranges, losing absolute precision in the process and using different internal hardware.

Board 2 yielded the result shown in Fig. 24.

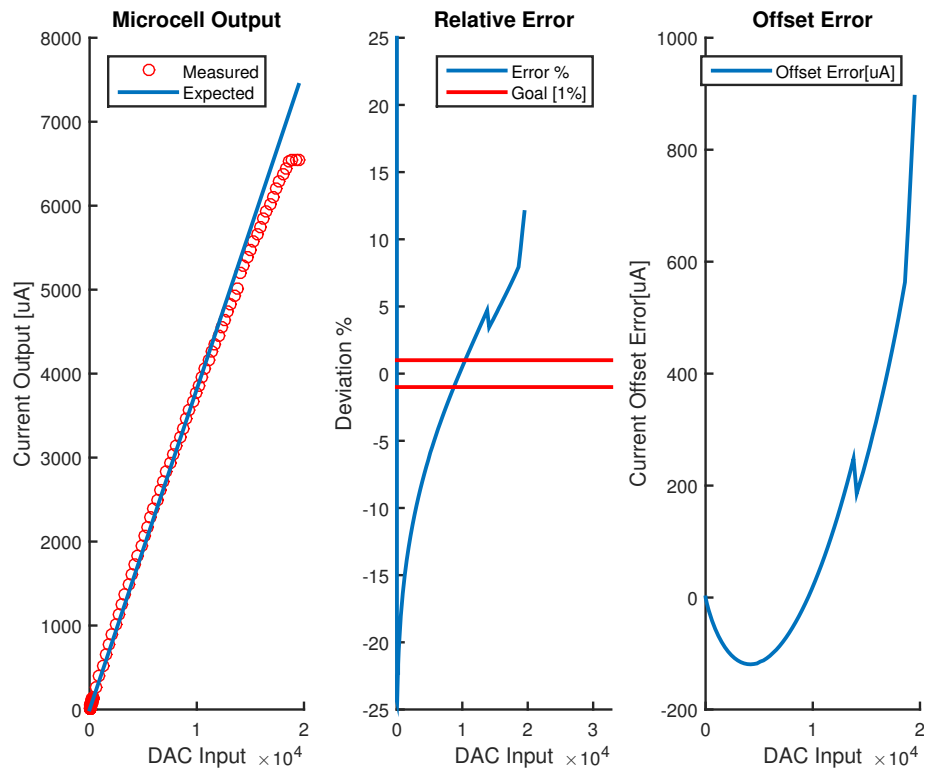


Figure 24: Micro-cell with mirror on board 2

The result is very similar to that from board 1, with the same saturation, non-linear errors and measurement artifacts.

6.4 Micro-Cell Without Mirror

Results from the micro-cell without the current mirror are presented here. Here the mirror IC has been removed and a $0\ \Omega$ bypass resistor has been soldered into place to short past the current mirror footprint. The resulting circuit is shown in Fig. 25. The micro-cell in this configuration was measured by utilising the GWINSTEK GDM-8341 5-1/2 benchtop multimeter in current measurement mode and a lab power supply PL303QMD applying 2V to the input of the Athol system, connected through the benchtop multimeter.

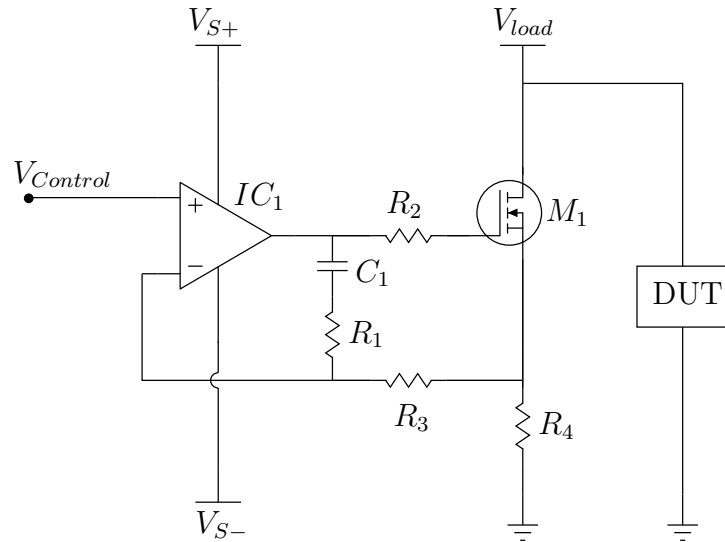


Figure 25: Micro-cell with the current mirror bypassed

Board 1 yielded the following results. Fig. 26 shows the expected and measured output, relative error between them and the absolute offset error difference.

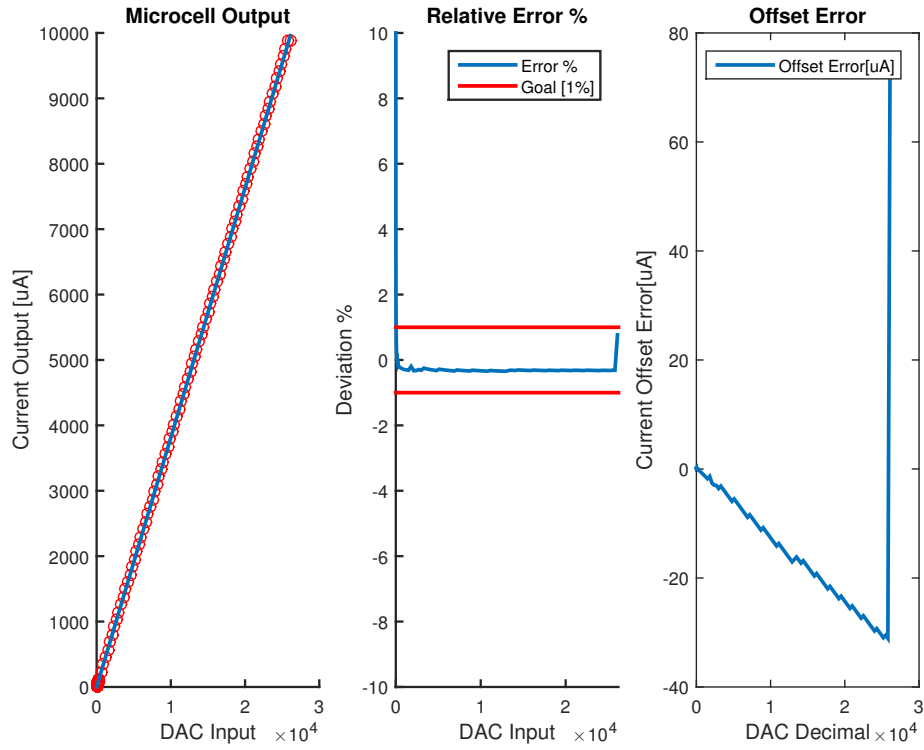


Figure 26: Micro-cell without mirror on board 1

The expected and measured results match very closely on visual inspection. Furthermore, the relative error is well within range for almost the entire dynamic range except at the beginning where a small offset exists. At count 13 the error is within the 1% limit. The jump in relative error right at the end is when the control voltage reaches the input voltage and saturation starts to take place. The full 10 mA dynamic range is covered in this configuration.

Note that there are no strong non-linear errors present, the absolute error is linear besides measurement noise and the saturation at the end. The linear absolute error indicates the presence of a gain error, which means a simple calibration for the offset in the beginning and gain error over the range can result in an even greater accuracy.

Board 2 yielded the following results, shown in Fig. 27. The expected and measured output, relative error and absolute offset error are shown like before.

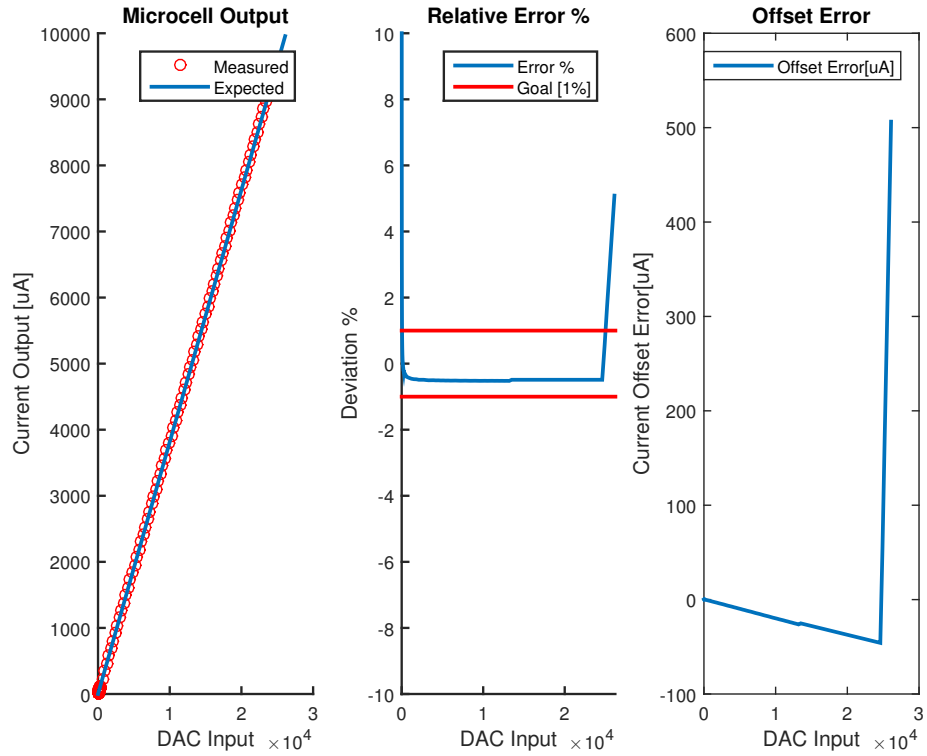
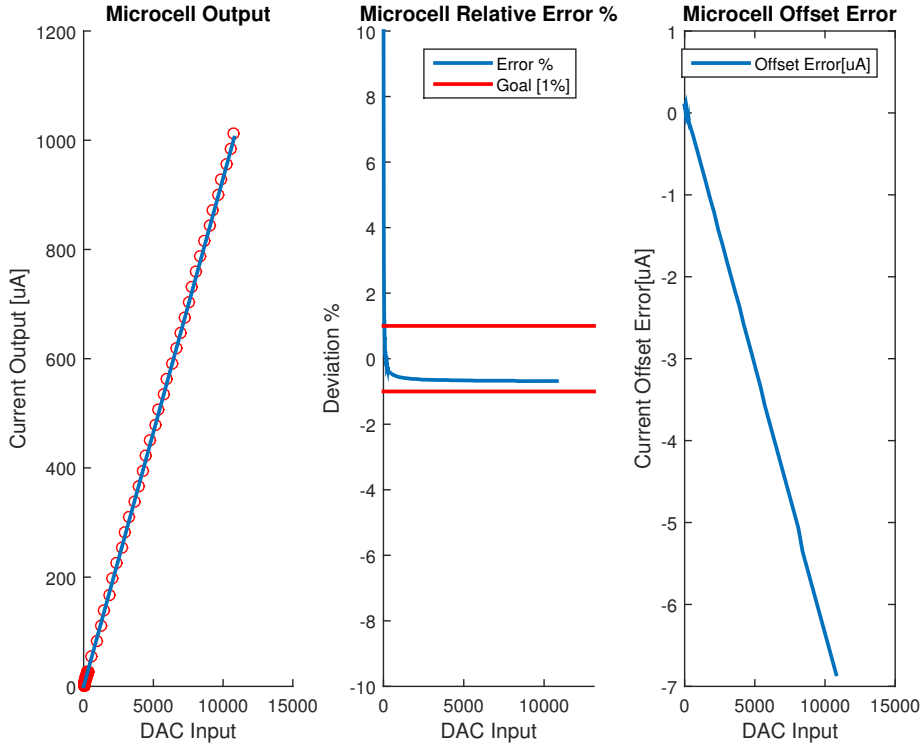


Figure 27: Micro-cell without mirror on board 2

The results are similar to the ones for board 1. On count 13, the error is within 1% and stays that way over the entire dynamic range, except at the end when saturation takes place as expected. The absolute offset error grows linearly indicating a simple gain error.

A third measurement was made on board 1 with the current setting resistor modified to decrease the current step size. It was modified from $200\ \Omega$ to $820\ \Omega$. This makes offset calibration to the smallest values supported by the GUI easier and more precise, making it easier to calibrate the offset away to meet the required accuracy for the $1\ \mu\text{A}$ specification accuracy. Fig. 28 shows the expected and measured output, relative error and absolute offset error like before.


 Figure 28: Board 1, with current setting resistor resised to $820\ \Omega$

When the resistor is increased, the dynamic range is reduced, but higher precision is attained.

6.5 Calibrated Results

Shown in Fig. 29 is the result of calibrating in software for the offset and gain errors of the load-cells, and measuring the expected values set in the graphical user interface to the measured at the input of the Athol hardware port. This measurement measures the contribution of both load-cells over the entire $0 - 250\text{ mA}$ combined dynamic range. The gain constants that were calculated are shown in Table 4. This result uses the modified $820\ \Omega$ resistor in the micro-cell.

Table 4: Gain Correction Constants for board 1

Parameter	Macro-cell	Micro-cell
Gain Correction	0.994157	0.99271
Offset Correction	0	1

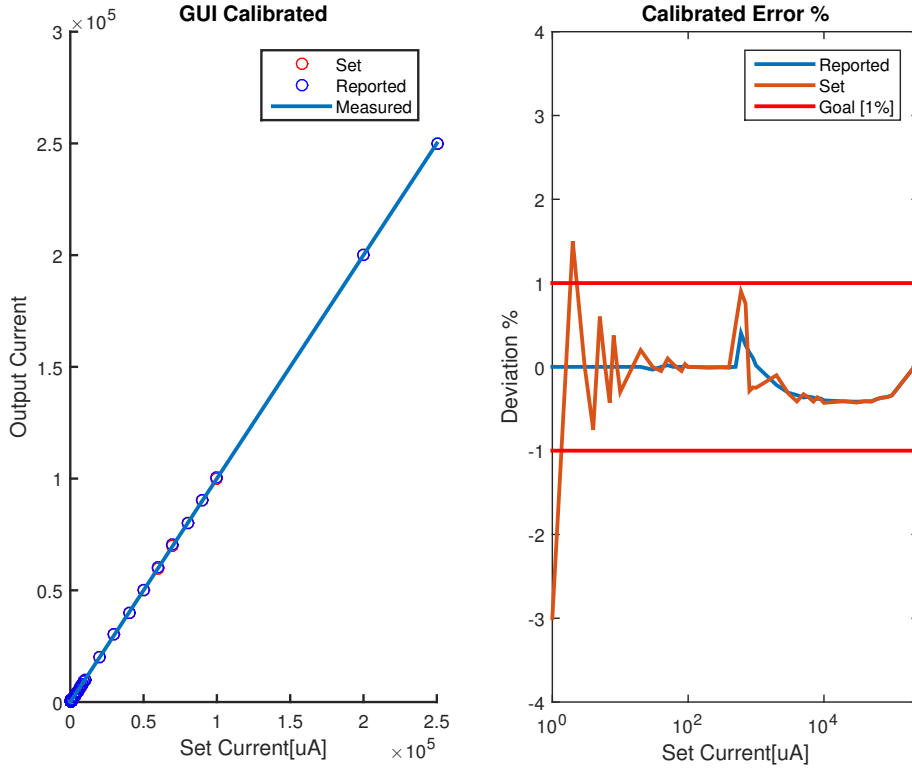


Figure 29: Performance after calibration in software

Due to the DAC and the discrete nature of the hardware, it is not possible to set the current to every desirable value, but only a number allowed by the discrete steps of the DAC. The software finds the closest value that corresponds to the current desired by the user and a quantisation error occurs. The left side of Fig. 29 shows the set current, reported and measured, which are too close to discern but shows that the transfer function is correct. The right side displays the relative error on a log scale on the x-axis. The errors are of two types: the error between the real value and the value the user attempted to enter, and then the error between the value the software reported using, and the real measured value.

It is evident that the measured and reported currents are extremely accurate for the micro-cell and within the measurement capability of the GWINSTEK GDM-8341, which is 10 nA. The set current is also within the 1% bounds except for the first two values, which are still within 5 percent as dictated by the specification for the smallest current supported by the GUI of 1 μ A. When the larger, less accurate, macro-cell takes over around the 500 μ A mark, a non-linear error is seen but the accuracy stays within bounds.

6.6 Leakage Current

The leakage current was estimated with two methods. First with a GWINSTEK GDM-8341 5-1/2 digit multimeter, PL303QMD Quad-mode dual channel power supply and a 10 M Ω resistance. The resistor was connected in series between the positive input and the power supply applying a test voltage so that any leakage current would create a voltage drop over the resistor. A test voltage of 9 V was applied to the input with the two load-cells turned off, and the voltage was measured over the resistor. Due to the extremely low voltage measured, a substantial amount of noise was seen in the measurement, making a reading off the display with precision difficult. The voltage over the resistor was approximately 300 μ V and it scaled down as the input voltage from the power supply was lowered, as expected for leakage current. This voltage indicates a leakage current of 300 pA was flowing through the resistor with a 9 V input voltage.

The second method used the 10 nF capacitor at the input, by charging it to a known voltage with the power supply, then disconnecting it and watching the ADC reading until it reached a lower voltage, tracking the time in between. Using the capacitor equation,

$$I = C \cdot \frac{dV}{dT}, \quad (5)$$

the leakage current was estimated to be 277 pA, which is in line with the previous result.

Leakage currents under 10 nA are further supported by the GWINSTEK GDM-8341 showing a zero current reading when attempting to measure the leakage current with it; the GDM-8341 has a 10 nA resolution.

6.7 Rise and Fall Time

The rise and fall time for the load cells was measured with a Tektronix TDS2014B oscilloscope, while switching the input current waveform with a square wave. A series resistor was connected between the input port of Athol and a PL303QMD power supply supplying the current. The oscilloscope measured the voltage drop over the resistor. The results are found in Table 5.

Table 5: Response times for loadcells

Parameter	Macro-cell	Micro-cell
Rise time	41.53 μ s	24.16 μ s
Fall Time	42.1 μ s	25.43 μ s

These rise and fall times constitute a bandwidth of 13 kHz and 8.3 kHz for the micro-cell and the macro-cell, respectively.

6.8 Timing Jitter

Jitter was measured by having Athol draw a approximately 200 Hz square wave current signal from the input, while a $100\ \Omega$ resistor was connected in series between the power supply (PL303QMD) and the input. The voltage over the resistor was monitored on a Tektronix TD2014B oscilloscope set to unlimited persistence to monitor jitter effects. The oscilloscope was configured to trigger on both edges of the waveform.

Fig. 30 shows the timing jitter when no user activity is present, and default processes and programs, in addition to the test script, are running. We call it the idle jitter, it is shown in Fig. 30. The waveform is relatively good looking, despite some jitter effects around the switching edges, amounting to about $300\ \mu\text{s}$ peak to peak.

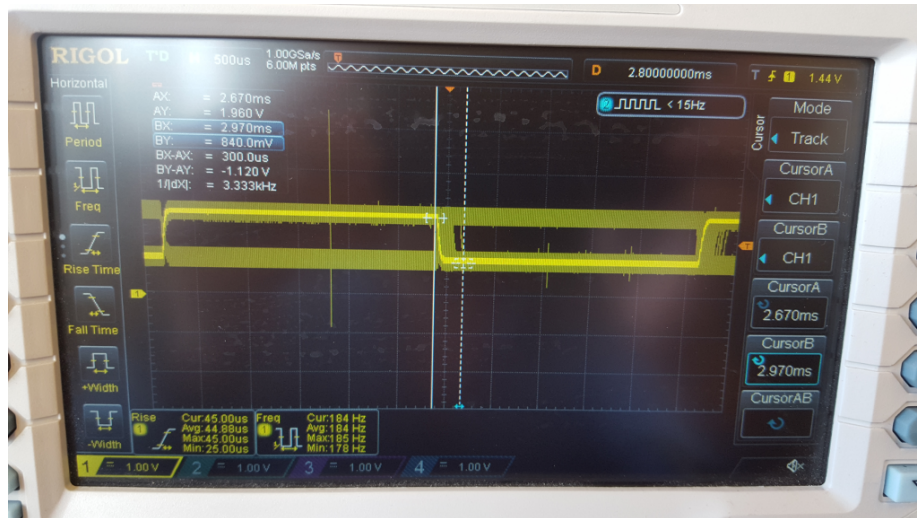


Figure 30: Idle timing jitter

Fig. 31 shows the same measurement, but with the trigger set to the rising edge (note the trigger point is outside of view on the scope display), and looking at the falling edge, and when the Raspberry Pi is under heavy load, i.e. receiving user input such as mouse movement and keyboard strokes, printing something to the console and running several Python calculation loops in parallel. The active mode jitter is shown in Fig. 31. The figure shows stronger timing jitter effects, with worst case jitter amounting to little over $2\ \text{ms}$ past target.



Figure 31: User activity timing jitter

6.9 Power Integration

Athol has support for integrating the instantaneous power to show the total power consumed by the load-cells. To test this functionality, a $47\ \mu\text{F}$ electrolytic capacitor was charged to approximately 1 V and discharged through the Athol hardware. According to the capacitor formula (equation 5), the energy contained in the capacitor should be approximately $23.5\ \mu\text{W}$. The outcome of the measurement was $20.3\ \mu\text{W}$, which is not far from the expected value. The differences are likely partially found in inaccuracies of the trapezoidal integration, but the biggest contribution appeared to be the leakage through the electrolytic capacitor and the voltage meter, which turned to be quite significant, making precision measurement quite difficult.

6.10 Summary

Found here in Table 6 is a summary of the measured capability of the system.

Table 6: Summary of measurement results

Parameter	Result	Desired
ADC Input Voltage Range	0 – 8.5 V	10 V
Minimum Input Voltage	400 mV	100 mV
ADC Accuracy (uncalibrated)	2 %	<5 %
Macro-cell Average Accuracy (calibrated)	0.6 %	<1 %
Macro-cell Response Time	42 μ s	<100 μ s
Micro-cell Average Accuracy (calibrated)	0.0034 %	<1 %
Micro-cell Response Time	25 μ s	<100 μ s
Combined Input Current Dynamic Range	0 – 250 mA	0 – 250 mA
GUI Minimum Accuracy (calibrated)	3 %	5 %
GUI (Combined Cells) Average Accuracy (calibrated)	0.15 %	<1 %
Input Leakage Current	300 pA	<100 nA
Maximum Jitter (Userspace Implementation)	>2 ms	<100 μ s

Overall, the results look good. The only parameters that do not meet the intended target were the ADC input voltage range, whose range was limited slightly by the common-mode input voltage range not extending all the way to the 10 V supply rail. The jitter that limits the speed at which calculations can be run and values updated. Additionally, the minimum input voltage, which without the mirrors became higher than anticipated.

6.11 Evaluation of a Energy-Harvesting System

6.11.1 Piezo-Electric Material and The Drill

To get some experience using our energy-harvesting evaluation system for its intended purpose, a quick experiment was made. Piezo-electric material SEN-09196 [44] with proof mass was ordered, sold as a vibration sensor but as piezo-electric material capable of harvesting energy. The test setup was as follows. An integrated diode bridge was attached to the piezo-electric material to rectify its voltage output. The rectified output was connected across a 47 μ F and a 2.2 μ F capacitor to store the energy. The capacitor terminals were then connected to the input port of the Athol measurement system.

The piezo-electric material was fastened to the edge of a table with a heavy mass. To excite the piezo-electric material, a hexagon key was attached to a battery powered drill and it used to batter the piezo-electric material, as shown in Fig. 32.



Figure 32: Drill used to excite piezo-electric material

As expected, when the drill was used, energy was created and consumed by Athol. Athol was set to draw $1\mu\text{A}$ of current in constant current mode. It recorded the voltage, current and total power consumed. Before having Athol start consuming current, the material was excited to bring the stored capacitor energy up, so that a voltage of about 1.65V was over the storage capacitors, which was done in order to not start at a low power point of the piezo-electric material. Fig. 33 and Fig. 34 show the output data created by Athol.

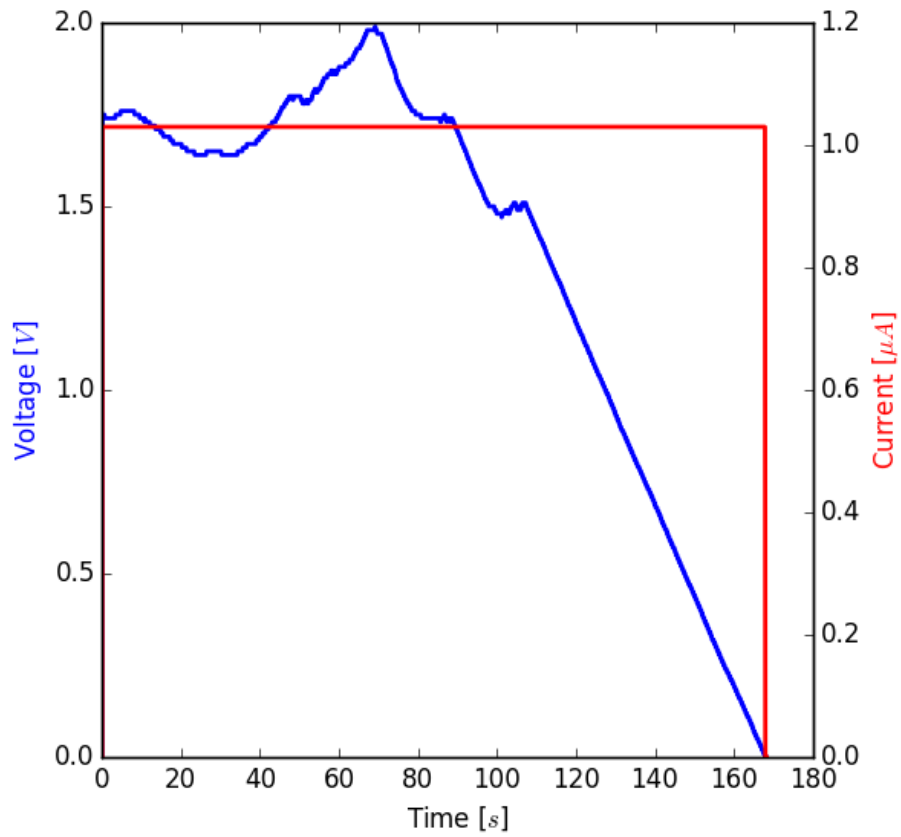


Figure 33: Drill used to excite piezo-material

The drill was capable of sustaining the voltage around the starting ≈ 1.7 V mark, supplying energy for the time period from 0 to 100 seconds, adding energy at a rate of approximately $1.7 \mu\text{W}$. After the 100 second mark the voltage falls consistently as the reserve energy is emptied out and no further energy is added.

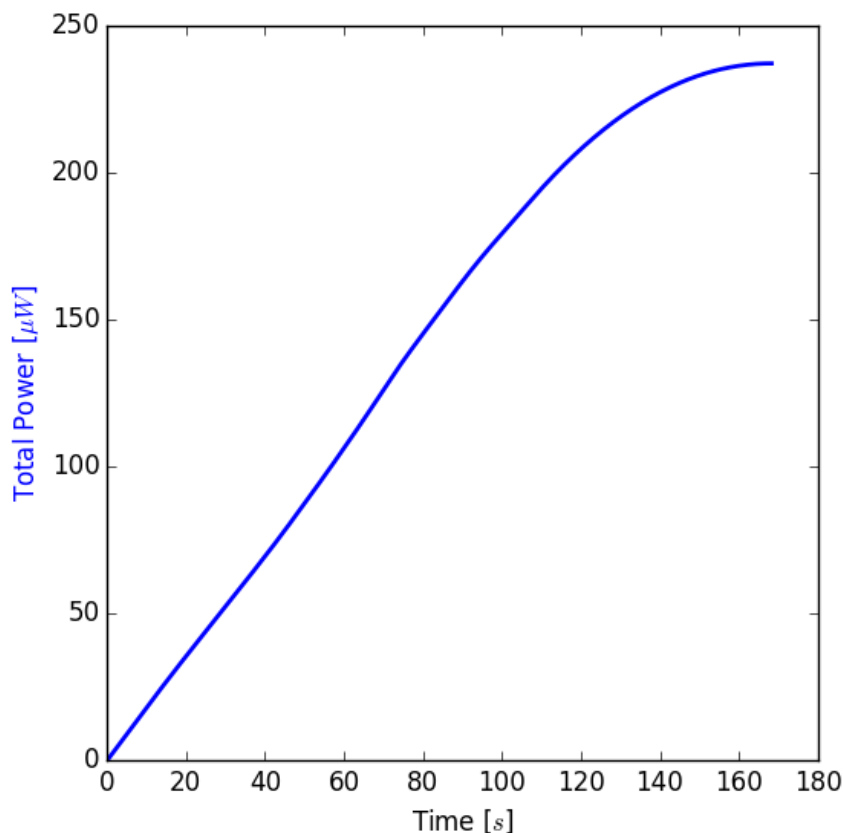


Figure 34: Total power harvested in drill experiment

The total energy harvested from the initial activity of getting the voltage up to about 1.7 V, running the drill on the piezo-electric material and emptying the reserve energy amounted to about $240 \mu\text{W}$.

Based on this observation, it can be concluded that battering a small vibration sensor with a drill, is not a very effective way of creating usable harvested energy. The resonant frequency of the piezo-electric material with proof mass is according to its datasheet on the order of 90 Hz, far from the capability of the drill used.

6.11.2 Piezo-electric Material on a Vibration Table

In an attempt to get closer to the resonance frequency of the piezo-electric material and therefore harvest more energy, another experiment was performed. In this experiment, the piezo-electric material was mounted on a plate which

was fastened on top of a vibration table using glue and reusable adhesive. The voltage from the piezo-electric material was rectified and stored in the same way as in the drill experiment. The vibration equipment setup is shown in Fig. 35.



Figure 35: Total and instantaneous power

The Athol hardware was connected to the energy-harvester setup via the capacitor terminals.

The vibration table was calibrated to vibrate at frequencies from 20 Hz up to 150 Hz in an attempt to find the resonance frequency of the piezo-electric material. This frequency, as specified in the datasheet for the material, was expected to be around 90 Hz. By sweeping the frequency, the resonance frequency was found to be around 27 Hz. This discrepancy is due to the way that the material was fastened to the vibration table. The eventual resonance frequency depends on the way it is fastened and the final proof mass size used.

The result of sweeping the frequency from 22 Hz to 30 Hz can be seen in Fig. 36. The acceleration of the oscillations was set to be $4g$. For the first 230 seconds of the experiment, approximately, the energy-harvester is not capable of sustaining the $1\mu\text{A}$ current that the Athol system is trying to draw from the capacitor. The Athol system recognises that the voltage is not high enough and keeps setting the current to zero as the voltage falls below a certain threshold. Around 230 seconds, corresponding to approximately 26 Hz the harvester begins harvesting more energy than Athol is taking out of the storage and as a result,

the voltage rises. The voltage keeps rising until when about 350 seconds have elapsed, at which point Athol begins drawing more energy from the storage than is being harvested. The excess energy is drained and at about 460 seconds, nothing remains and the $1\ \mu\text{A}$ current can no longer be sustained.

The frequency range at which the harvester was able to sustain constant current of $1\ \mu\text{A}$ is only from 26.17 Hz to 29.67 Hz.

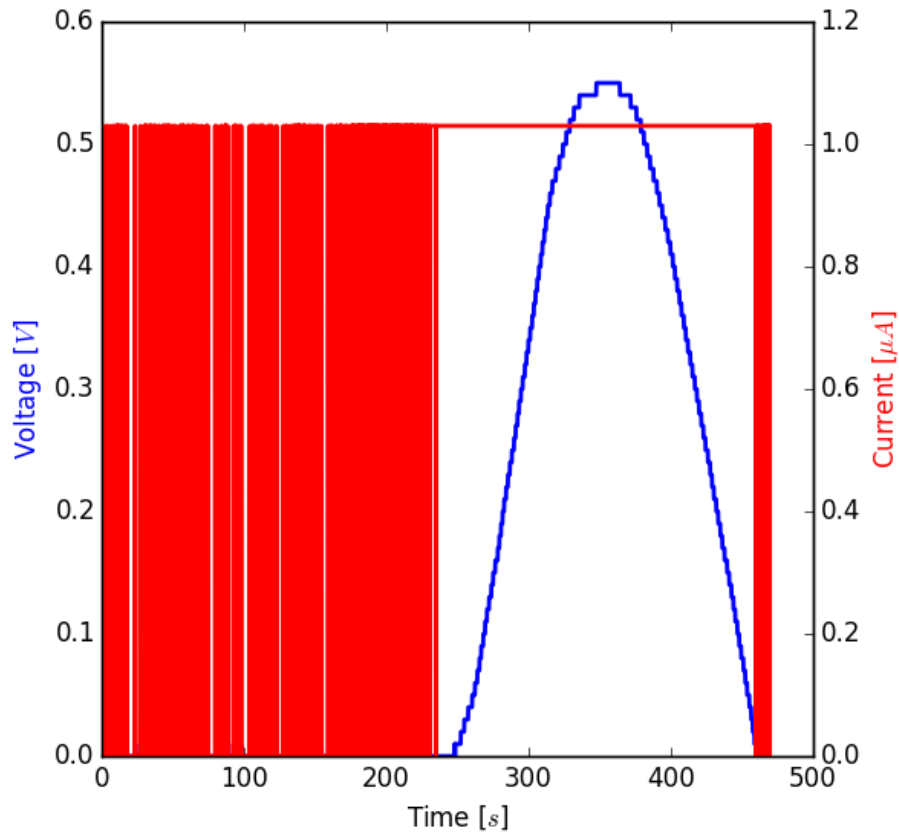


Figure 36: Voltage and current as a function of time in vibration experiment

The total power harvested during this experiment as a function of time can be seen in Fig. 37. The blue line shows the total power but the red one shows the first derivative of the total power. The total harvested power amounts to about $73\ \mu\text{W}$ over the duration of 200 seconds. By differentiating the total power curve, the maximum power input (hitting the resonance frequency) was obtained as $0.58\ \mu\text{W}\text{s}^{-1}$ at 350 s. This moment in time corresponds to a frequency of 27.67 Hz. This would be the maximum power when starting from approximately

zero volts.

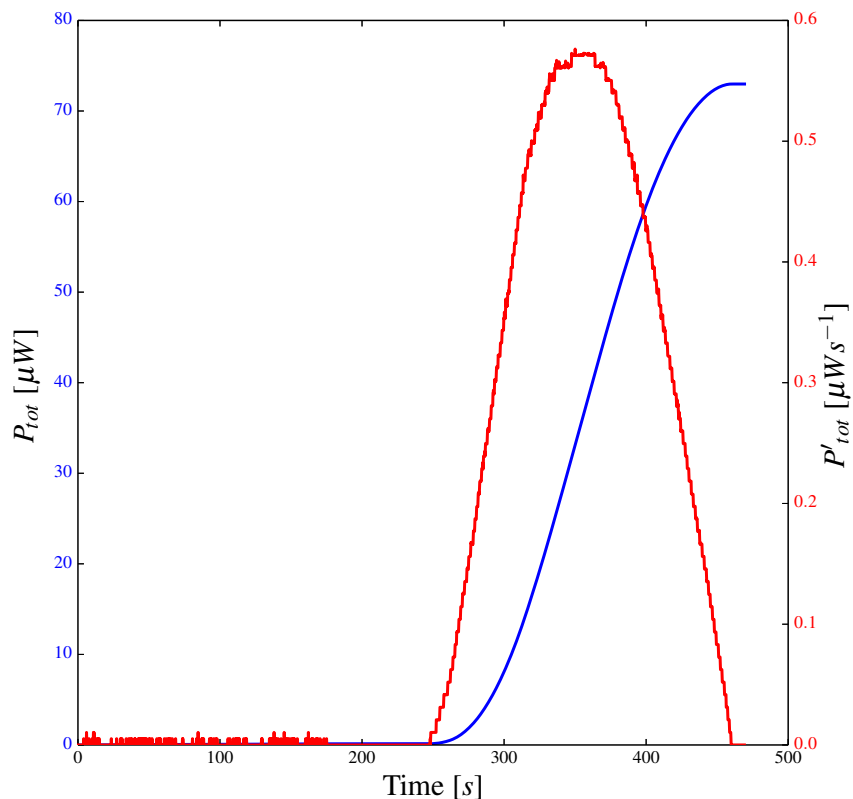


Figure 37: Total power harvested and its first derivative as a function of time in vibration experiment

An attempt to locate the absolute maximum power point for the setup was also performed. A few frequencies and loads were tested to see if a stable voltage developed with a fixed load, or if the energy reservoir would stay depleted or grow consistently. The test was performed by setting the vibration table to vibrate at the specified frequency, and Athol instructed to draw a constant current. This was done long enough for the voltage to settle for each measurement point, or if it was deduced that it would grow forever or stay at zero. The results are shown in Table 7 below.

Table 7: A few frequency and load combinations in an attempt to locate the maximum power point

Load[μ A]	Frequency[Hz]	Settling Voltage[V]	Power[μ W]
1.00	30	1.89	1.89
1.00	25	∞	N/A
2.00	25	3.02	5.95
3.00	25	0	N/A
2.00	22	0	N/A
2.00	23	0	N/A
1.00	23	∞	N/A

By doing these measurements, it was possible to establish very coarsely where the maximum power point resided in terms of frequency and load. At 25 Hz and drawing 2μ A the voltage settled to 3.02 V, drawing out 5.95μ W consistently. At the same frequency, load current of 1μ A resulted in the voltage building slowly up to the limit of the system and 3μ A collapsed the voltage entirely. The maximum power point lies thus between 1μ A and 2μ A. At the time of the experiment, the current step supported by the software was 1μ A. This step size is too coarse to precisely locate the power point for the small low power piezo-material used. The step size supported by the DAC is currently ≈ 100 nA and the result indicates that for small low power materials it would be beneficial to open the possibility for the software to utilise the maximum precision between the smallest steps to more precisely find where the maximum power point lies. The explanation for the difference in resonance frequency between the earlier sweep and this experiment is that the configuration was tampered with, which shifted the resonance frequency of the setup slightly.

7 Discussion

Here, selected points on how the system performed and what could have been better are discussed. Overall, the system performed as it was supposed to and after using it to evaluate an energy-harvesting system, the authors believe that the system is in fact a good solution to the problem formulated in chapter 1. Whether the system is usable in the field by professionals remains to be seen.

7.1 Current-Mirror Performance

The purpose of the mirror was to be able to draw current on the micro-cell at practically zero input voltage. Those gains never materialised due to the strong non-linearity and inaccuracy introduced after copying the reference current twice. It is very difficult to get matching good enough to support 1% copy of the reference current twice in succession. Even with an off-the-shelf matched IC, it did not work well enough to reach the specification. Non-linear errors are harder to compensate for and a decision was made to remove the current mirror entirely and rely on the bypassed version of the micro-cell.

7.2 Load-cells Combined

As the current range exceeded five decades the choice of creating two load cells, each designed for different ranges, turned out to be wise. The macro-cell did not turn on for currents under 300 μA , but when it did it performed better than expected, and with reduced input voltage requirements compared to the micro-cell for the same desired current. The micro-cell turned on for the lowest currents but could not cover the upper part of the required current without needing a minimum input voltage much higher than we specified due to the current mirror being removed.

Because the current mirror was removed, the limitation of the trans-impedance amplifier on the minimum input voltage came into effect. But by increasing the resolution of the micro-cell, and scaling the dynamic range down this effect was reduced. Furthermore, the macro-cell was able to take over sooner than anticipated as it proved to have the accuracy to take over well below the original estimate, thus reducing the control voltage disadvantage of the micro-cell. The reason for the different input voltage impact between the two cells is the loop gain and smaller current set resistor in the macro-cell, reducing the voltage needed to sink the maximum input current.

The switchover point was selected to be 500 μA , little over the 300 μA starting current for the macro-cell. At 500 μA the micro-cell needs a 0.4 V input voltage to function correctly, while at 500 μA the macro-cell only needs 500 μA to draw such current and peaks at 250 mV at 250 mA. If the micro-cell would be allowed to cover its full 10 mA range, it would need at least a 2.0 V input voltage at its highest current. The optimal switchover point is a point where both load-cells function, where the step size for the micro-cell is small enough

to support offset calibration at the lowest supported current in the GUI, and the control voltage for the micro-cell is minimized.

This arrangement scaled the 'maximum' minimum input voltage requirement, over the entire combined dynamic range, to 0.4 V. This is a bit higher than the targeted 0.1 V. The average required minimum input voltage is much lower however as it grows linearly from 0 V, to the limit over the current range of each cell. And in many applications this limitation is not expected to be a hindrance, as it is lower than many wireless sensors can utilise and the system adapts automatically to when it cannot sustain desired current due to too low an input voltage.

7.3 Minimum Input Voltage - Current Foldback

As the situation could arise, where the input voltage was below the minimum required to set a specified current, the opportunity for large errors was present unless Athol could scale back the current to a value supported by the input voltage. Similarly if there is no voltage at the input at all, no current can be drawn. By reading the input voltage through the ADC, it was possible to create usable feedback to verify that the voltage was indeed high enough to sustain the current desired, and dynamically scale the current so that no unintended errors are introduced in the power measurement if the voltage from the device under test collapses. For the drawn current to be valid, the input voltage seen at the input needs to be higher than

$$\frac{V_{control}}{\text{Loop}_{gain}} + V_{DS}, \quad (6)$$

where $V_{control}$ is the control voltage for the current cell, Loop_{gain} is the feedback loop gain (10 for the macro-cell, 1 for the micro-cell) and V_{DS} is the drain-source voltage of the pass-element MOSFET in the load-cells. The drain-source voltage headroom needed by the MOSFET is the $R_{ds,ON}$ resistance multiplied with the current, with the component choices made for Athol it adds about 125 mV to the minimum input voltage needed (0.25 V) at 250 mA for the macro-cell. It is insignificant for the micro-cell, due to the small currents.

7.4 Calibration

Calibration can be done in either the analog domain or in the digital domain. However, it is usually a bit more cumbersome to perform in the analog domain and harder to change, as it requires potentiometers or manual tweaking of resistor values, while only setting and changing magic numbers in a program in the digital domain. Athol supports both methods, but by setting the current step-size low enough, it was possible to tune the offset in the digital domain so that a offset adjustment could be picked to shift the output sufficiently close to the targeted $1 \mu\text{A}$ current to fulfill the specification. Furthermore, the gain error of the cells could be adjusted for, especially for the micro-cell which had very linear errors, to maintain exceptional accuracy over the dynamic range.

After calibration, the mean relative error was 0.0034 % from 23 samples for the micro-cell, between the measured and reported current in the GUI. It was 0.3 % for the macro-cell.

7.5 Timing Jitter

A Raspberry Pi running standard Linux, or any general purpose operating system for that matter, is not particularly well suited for real-time applications. Under normal circumstances, Linux is designed for throughput rather than determinism. The scheduler preempts tasks in a complex manner with tens or hundreds of tasks running at the same time, making analysis even more difficult. Furthermore, garbage collectors in managed languages like Python will stop applications while garbage collection takes place, producing sudden halts in program execution until it is finished. These effects, and the nature of the standard operating system, results in noticeable timing jitter, meaning that the time between events that are expected to happen periodically is actually distributed randomly in time around the expected periodic value.

This effect can be clearly seen in our jitter measurements in Fig. 31 and in Fig. 30. It can be concluded though that the effects are not large enough to affect measurements very strongly at sampling speeds of 10 Hz, but at higher sampling speeds such as 100 Hz, the jitter approaches 20 %. The sampling speed, as referred to here is the rate at which the Athol software performs communication with the hardware and performs calculations to yield usable results.

A tick rate of 10 Hz will be sufficient for manual sweeping and testing of harvesting systems, as storage mediums for energy-harvesting designs are assumed to contain a reasonable buffer to maintain voltages relatively constant on such small timescales. However, it will not be enough to emulate current profile of sensors down to their sleep cycles at 100 – 1000 Hz. Emulating sensors is still possible, but only if currents are averaged to higher timescales, which means recorded or estimated sensor power consumption needs to be modified to reflect that before being used as a data-set for the current implementation.

7.6 Total Power Calculations

As was explained in chapter 5, an approximation of the total power drained from a system under test is calculated by using the trapezoidal rule (equation 4). The reason why this method was chosen is because it is computationally simple and can be used to continuously calculate the total power drawn in an ongoing test. However, this method is not particularly accurate when the input is changing rapidly and the total-power obtained should not be considered to be exact.

Other, more accurate, integration methods exists and one or more of them could be used in post-processing of the data logged by Athol in an attempt to produce more accurate total-power values.

8 Conclusion

The problem that was to be solved in the thesis was to enable the evaluation of piezo-electric, electro-magnetic and radio-frequency energy-harvesting systems, that are to power wireless and battery-less sensors. This was done with the purpose of gaining insight into the design, performance and validation aspect of the environment-harvester-sensor dynamic at the circuit level. The work milestones reached were the pre-study being performed, the specification synthesis performed, the system designed according to the specification and finally the evaluation of the complete system by having it evaluate an energy-harvesting system in two experiments.

As is supported by the results and testing and is the understanding of the authors, the Athol measurement system has decent evidence for the hardware and software being functionally correct. Athol to the most part conforms to the specification as originally crafted, to the point at least where it certainly can be concluded to be an accurate instrument in sinking controlled currents and drawing controlled power levels from a connected energy source. Even though full conformity to the specification was not reached, it did not really matter in the end when it came to usability, some of shortfalls can be easily adjusted for as well, such as the input voltage range.

The piezo-electric material experiments with the drill and the vibration table demonstrate that we can use the system to evaluate how much energy enters a storage element, both the total energy and a estimate of the energy supplied over time. Furthermore, the emulation feature, not demonstrated specifically in the thesis text, due to time concerns, can emulate sensors over time and from the data produced, it should be discernible if the storage element voltage ever collapses to the point of risking system integrity.

In the thesis, we researched and found common characteristics of energy-harvesting systems targeted for wireless sensors. The similarities were found in rectification, power conditioning and output of harvested energy into a energy reservoir, which we argued to be most commonly a capacitor. From that we were able to craft a specification to a test system that managed to fulfill to the most part our design choices. Furthermore, the system proved to be usable to evaluate a energy-harvesting system, albeit a crude one, but one none-the-less, harvesting minuscule amounts of power. Even though only a piezo-electric energy-harvesting system was evaluated, the general purpose nature and similarity in the output side of these systems means electro-magnetic and radio-frequency based harvesters should be capable of being evaluated by Athol as well.

9 Future Work

Possible future improvements to the system are discussed here below.

9.1 Improving Jitter to Improve Speed

In the current implementation the jitter is a bottleneck to reaching the bandwidth stated in the specification. The jitter problem can be reduced by creating a special kernel driver to control the hardware directly and buffer the data. Kernel drivers are written in C in Linux and are not garbage collected like the Python programming language, furthermore they can utilise hardware queueing and have higher priorities than user-space applications when it comes to scheduling, reducing OS and user generated jitter effects. It is uncertain whether a kernel driver implementation will reach the bandwidth stated in the specification.

Another way to reduce jitter would be to add a micro-controller to the hardware, sitting between the DAC/ADC and the Raspberry Pi. Its purpose would be to buffer the input and output data and control the DAC and the ADC with less jitter than what is possible with the Raspberry Pi. This approach would complicate the communications between the Raspberry Pi and the hardware, but is most assuredly capable of reaching low enough jitter to support the bandwidth as specified, as software can be specialised and run with little or no interruption from unrelated activities.

9.2 Potential For Higher Resolution

Given the very high precision acquired after calibration for the micro-cell, the possibility is present to further increase the accuracy by either sacrificing maximum-minimum input voltage for smaller current steps with the same DAC, or increase the resolution of the DAC to make smaller changes to the control voltage. It became obvious after one of the experiments that unlocking the higher resolution in the software would be useful, but whether higher resolution over what is supported by the DAC itself is useful is not fully clear at this moment, but a 20-bit DAC instead of a 16-bit one may be able to increase the GUI supported minimum current from 100 nA down to under 10 nA, which would still yield a leakage current under 5% of the smallest supported current step and allow higher precision in locating maximum power points of very small piezo-electric energy-harvesters.

9.3 Constant Voltage Mode

The current version of the Athol software does not have the ability to draw current in such a way that the load voltage remains constant. It became clear while performing the vibration table experiment that such a mode would be helpful for determining the maximum power point of an energy-harvester setup as it would make sure that any power exceeding the level corresponding to the

set voltage would be absorbed. It is possible to locate the maximum power point using the current version without the feature, but it is more time consuming and takes some guesswork as it is.

9.4 Generalisation of the Thesis Work

Even though the Athol system has been designed to evaluate three specific energy-harvesting technologies, namely piezo-electric harvesting, electro-magnetic harvesting and radio-frequency harvesting, it can most likely be used for other energy-harvesting technologies as well, such as solar harvesting, thermoelectric harvesting and possibly others. The reason for this is that harvesters for these methods can in theory also be designed to charge supercapacitors or output voltages and currents within the capability of Athol. As Athol is in essence a precision, mobile active load, it can in theory be used to evaluate small power supplies. It could perhaps be useful for evaluating micro-power power-supplies that can only supply very small currents for micro-electronics, as it has the capability to accurately draw small currents down to single micro-Amperes. Whether there is need for such capability is unknown.

References

- [1] *Syntronic AB*. URL: <http://www.syntronic.com/index.php/about-us/>.
- [2] A. Khaligh, P. Zeng, and C. Zheng. “Kinetic Energy Harvesting Using Piezoelectric and Electromagnetic Technologies—State of the Art”. In: *Industrial Electronics, IEEE Transactions* 57 (3 2009), pp. 850–860. DOI: 10.1109/TIE.2009.2024652.
- [3] M. Piñuela, P.D. Mitcheson, and S. Lucyszyn. “Ambient RF Energy Harvesting in Urban and Semi-Urban Environments”. In: *Microwave Theory and Techniques, IEEE Transactions on* 61.7 (July 2013), pp. 2715–2726. DOI: 10.1109/TMTT.2013.2262687.
- [4] T. B. Lim, N. M. Lee, and B. K. Poh. “Feasibility Study on Ambient RF Energy Harvesting for Wireless Sensor Network”. In: *Microwave Workshop Series on RF and Wireless Technologies for Biomedical and Healthcare Applications (IMWS-BIO), 2013 IEEE MTT-S International* (2013), pp. 1–3. DOI: 10.1109/IMWS-BIO.2013.6756226.
- [5] S. Sudevalayam and P. Kulkarni. “Energy Harvesting Sensor Nodes: Survey and Implications”. In: *Communications Surveys & Tutorials, IEEE* 13.3 (2010), pp. 443–461. DOI: 10.1109/SURV.2011.060710.00094.
- [6] Texas Instruments. *SimpleLink ultra-low power wireless MCU for BLE (Bluetooth Smart)*. 2016. URL: <http://www.ti.com/product/cc2640> (visited on 06/23/2016).
- [7] J. Yick, B. Mukherjee, and D Ghosal. “Wireless sensor network survey”. In: *Computer Networks* 52 (12 2008), pp. 2292–2330. DOI: 10.1016/j.comnet.2008.04.002.
- [8] S. Chalasani and J.M. Conrad. “A survey of energy harvesting sources for embedded systems”. In: *Southeastcon, 2008. IEEE*. Apr. 2008, pp. 442–447. DOI: 10.1109/SECON.2008.4494336.
- [9] S. Sudevalayam and P. Kulkarni. “Energy Harvesting Sensor Nodes: Survey and Implications”. In: *Communications Surveys Tutorials, IEEE* 13.3 (Mar. 2011), pp. 443–461. DOI: 10.1109/SURV.2011.060710.00094.
- [10] D. Spreemann and Y. Manoli. *Electromagnetic Vibration Energy Harvesting Devices: Architectures, Design, Modeling and Optimization*. English. 1. Aufl. Vol. 35. Dordrecht: Springer Netherlands, 2012.
- [11] W. G. Nelson. *Piezoelectric Materials*. English. Nova Science Publishers, Inc., 2010.
- [12] R. S. Dahiya and M. Valle. *Robotic tactile sensing: technologies and system*. English. 1. Aufl.;1;2013; Dordrecht;New York; Springer, 2013;2012;2014;2015;
- [13] S. Roundy, P. K. Wright, and J. M. Rabaey. *Energy Scavenging for Wireless Sensor Networks: with Special Focus on Vibrations*. English. Boston, MA: Springer US, 2004.

- [14] Powercast Corporation. *Powercast: Wireless Power for a Wireless World*. 2016. URL: <http://www.powercastco.com/> (visited on 04/08/2016).
- [15] T. Eswam and P. L. Chapman. "Comparison of Photovoltaic Array Maximum Power Point Tracking Techniques". In: *IEEE Transactions on Energy Conversion* 22.2 (June 2007), pp. 439–449.
- [16] A. S. Sedra and K. C. Smith. *Microelectronic circuits*. English. 6., international. Oxford;New York; Oxford University Press, 2011.
- [17] Wikipedia. *Operational transconductance amplifier*. 2016. URL: https://en.wikipedia.org/wiki/Operational_transconductance_amplifier (visited on 17/05/2016).
- [18] Analog Inc. *Op amp basics*. 2016. URL: http://www.analog.com/library/analogDialogue/archives/39-05/Web_Ch1_final_R.pdf (visited on 17/05/2016).
- [19] F. Maloberti. *Data converters*. English. Dordrecht, Netherlands: Springer, 2008;2007;
- [20] Wikipedia. *Digital to analog converter*. 2016. URL: https://en.wikipedia.org/wiki/Digital-to-analog_converter (visited on 17/05/2016).
- [21] Texas Instruments. *Understanding Data Converters*. 2016. URL: <http://www.ti.com/lit/an/slaa013/slaa013.pdf> (visited on 17/05/2016).
- [22] Wikipedia. *Analog to digital converter*. 2016. URL: https://en.wikipedia.org/wiki/Analog-to-digital_converter (visited on 17/05/2016).
- [23] S. Chalasani and J. M. Conrad. "A survey of energy harvesting sources for embedded systems". In: *Southeastcon, 2008. IEEE*. Apr. 2008, pp. 442–447. DOI: 10.1109/SECON.2008.4494336.
- [24] Mide Inc. *Mide*. 2016. URL: <http://www.mide.com/> (visited on 04/05/2016).
- [25] Piceramic Inc. *Piceramic*. 2016. URL: <http://www.piceramic.com/> (visited on 04/05/2016).
- [26] Revibe Energy. *Revibe Energy*. 2016. URL: <http://revibeenergy.com/> (visited on 04/06/2016).
- [27] Perpetuum Inc. *Perpetuum*. 2016. URL: <http://www.perpetuum.com/> (visited on 04/06/2016).
- [28] T. Le, K. Mayaram, and T. Fiez. "Efficient Far-Field Radio Frequency Energy Harvesting for Passively Powered Sensor Networks". English. In: *IEEE Journal of Solid-State Circuits* 43.5 (2008), pp. 1287–1302.
- [29] Freevolt. *Freevolt Air Pollution Smart Sensor*. 2016. URL: <https://our.clean.space/> (visited on 18/05/2016).
- [30] Freevolt. *Freevolt Technology*. 2016. URL: <http://www.draysontechnologies.com/newsarticle.html?DRAYSON-TECHNOLOGIES-UNVEILS-BREAKTHROUGH-RF-ENERGY-HARVESTER-FREEVOLT-5> (visited on 18/05/2016).

- [31] The Raspberry Pi Foundation. *Raspberry Pi - Teach, Learn and Make with Raspberry Pi*. 2016. URL: <https://www.raspberrypi.org/> (visited on 06/23/2016).
- [32] Texas Instruments. *LMC6041 Precision Amplifier*. 2016. URL: <http://www.ti.com/product/LMC6041> (visited on 06/24/2016).
- [33] Texas Instruments. *MPC3201 12b ADC*. 2016. URL: <http://www.microchip.com/wwwproducts/en/MCP3201> (visited on 06/24/2016).
- [34] Texas Instruments. *OPA277 Op-amp*. 2016. URL: <http://www.ti.com/product/OPA277> (visited on 06/24/2016).
- [35] Texas Instruments. *LTC2051 Zero Shift Op-Amp*. 2016. URL: <http://www.linear.com/product/LTC2051> (visited on 06/24/2016).
- [36] Python Software Foundation. *Python*. 2016. URL: <https://www.python.org/about/> (visited on 05/02/2016).
- [37] Nokia. *PySide: Python for Qt*. 2016. URL: <http://www.pyside.org/> (visited on 05/02/2016).
- [38] The Qt Company. *The Qt Project*. 2016. URL: <https://www.qt.io/about-us/> (visited on 05/02/2016).
- [39] G. E. Krasner and S. T. Pope. "A Cookbook for Using the Model-View-Controller User Interface Paradigm in Smalltalk-80". English. In: *Journal of Object-Oriented Programming* (1988), pp. 26–49.
- [40] J. D. Hunter. "Matplotlib: A 2D graphics environment". In: *Computing In Science & Engineering* 9.3 (2007), pp. 90–95.
- [41] J. Stoer and R. Bulirsch. *Introduction to Numerical Analysis*. English. Third. Vol. 12. New York, NY: Springer New York, 2002.
- [42] Ltd Good Will Instrument Co. *GDM-8341 Benchtop Digital Multimeter*. 2015. URL: http://www.gwinstek.com/en-global/products/Digital_Meters/Benchtop_Digital_Multimeters/GDM-8342_GDM-8341 (visited on 06/23/2016).
- [43] Aim and Thurlby Thandar Instruments. *PL Series DC Power Supplies - PL303QMD*. 2016. URL: <http://www.aimtti.com/product-category/dc-power-supplies/aim-plseries> (visited on 06/23/2016).
- [44] Sparkfun. *SEN-09196 piezo material*. 2016. URL: <https://www.sparkfun.com/products/9196> (visited on 06/24/2016).

A Calculations and Derivations

Various calculations and derivations that are omitted in the thesis itself are listed below.

A.1 ADC

A.1.1 Resolution

The resolution of the MCP3201 is 12 bits. With a dynamic range of 5 V, the voltage resolution is

$$\frac{V}{2^b} = \frac{5V}{2^{12}} = 1.2mV \quad (7)$$

A.1.2 Noise and SNR

The noise seen by the ADC is the input referred noise of the operational amplifier. The thermal noise of resistors is ignored as they are assumed not large enough to be significant. According to the data sheet the input referred noise is $0.22\mu V$ for frequency $0.1 - 10$ Hz and approximately $10nV/\sqrt{Hz}$ after that. With a dynamic input voltage range of 5 V the signal-to-noise ratio (SNR) is, assuming a single pole anti aliasing filter with 10 kHz bandwidth,

$$\begin{aligned} & 10 \cdot \log_{10} \left(\frac{\text{Signal}^2}{\text{Noise}^2} \right) \\ &= 10 \cdot \log_{10} \left(\frac{\frac{(10V)^2}{2}}{(0.22\mu V)^2 + (10nV \cdot \sqrt{10kHz} \cdot 1.57)^2} \right) \quad (8) \\ &= 134.9dB \end{aligned}$$

This indicates that noise is a insignificant factor contributed by the operational amplifier.

A.1.3 Offset Error

The offset of OPA277 varies between part numbers, lowest is $10\mu V$ with a $0.1\mu V$ per degree Celsius drift. This amounts to a $16\mu V$ error over the desired temperature range. This error yields a resolution corresponding to

$$\log_2 \left(\frac{Fullscale}{Offset} \right) = \log_2 \left(\frac{5V}{16\mu V} \right) = 18.25bits, \quad (9)$$

indicating that op-amp offset does not affect the ADC accuracy significantly.

A.2 DAC

A.2.1 Noise

The bandwidth desired is 10 kHz. The noise density of the DAC is $18 \text{ nV}/\sqrt{\text{Hz}}$. Assuming a single pole filter at the output, the SNR is

$$10 \cdot \log_{10} \left(\frac{\text{Signal}^2}{\text{Noise}^2} \right) = 10 \cdot \log_{10} \left(\frac{\frac{(5V)^2}{2}}{(18 \text{ nV} \cdot \sqrt{10 \text{ kHz}} \cdot 1.57)^2} \right) = 123.9 \text{ dB}, \quad (10)$$

corresponding to approximately 20 bits, well within the accuracy needed. The OPA277, which is the final input voltage to the load cells has a noise density that amounts to over 20 bits as shown earlier, and offset equivalent of over 18 bits resolution, meaning that the final control voltage will fulfill close to 16 bits effective DC accuracy.

A.2.2 Voltage reference

Accuracy and drift of the voltage reference will affect accuracy of the DAC. MAX6002 was found as a suitable candidate with initial accuracy of $\pm 1\%$ and noise levels of $60 \mu\text{V}$ Pk-Pk @ $0.1 - 10 \text{ Hz}$ and $125 \mu\text{V}$ RMS at 10 Hz to 10 kHz and drift of $100 \text{ ppm}/^\circ\text{C}$. This corresponds to an estimated maximum DC error per step of

$$\frac{E_{\text{offset}} + E_{\text{drift}}}{2^b} = \frac{2.5 \cdot 0.01 + 2.5 \cdot 100 \cdot 10^{-6} \cdot 45^\circ\text{C}}{2^{16}} = 0.38 \mu\text{V}, \quad (11)$$

where b is the number of bits. The noise contribution is a very small addition compared to the DC error and is negligible. A per-step error of $0.38 \mu\text{V}$ is less than half a percent of the smallest step size.

A.3 Loadcells

A.3.1 Micro-cell - Dynamic Range

The maximum current is limited by the common mode input voltage range of the amplifier, supply voltage rails, size of current set resistor and MOSFET threshold voltages. This assumes mirrors and the operational amplifier share the same positive supply rail. The maximum current supported will be the minimum quantity yielded when considering all the contributions, demonstrated by the equation

$$I_{\text{max}} = \min \left(\frac{V_{\text{control}}}{R_4}, \frac{V_{\text{supply}} - V_{CM}}{R_4}, \frac{V_{\text{supply}} - V_{THM1} - V_{THM2}}{R_4} \right) \quad (12)$$

For the thesis design, the smallest quantity yielded out of 12 is due to the 2.5 V limited range of V_{control} . Setting the current limit as 10 mA for the micro-cell, assuming a 200Ω current setting resistor.

The lower limit, excluding the off state zero current, is governed by the errors allowed at the smallest current step, the amplifier offset voltage V_{OS} and its drift V_{drift} with temperature from ambient, the input referred noise of the operational amplifier V_N , input bias current, and size and accuracy of the current set resistor. The average relative accuracy will be largely set by the precision of the current set resistor. The minimum current usable, set by the lowest absolute error requirement of 5% will be, with noise in peak to peak voltages.

$$\begin{aligned}
 I_{min} &= \frac{1}{E_{max}} \cdot \left(\frac{V_N + V_{OS} + V_{drift} \cdot \Delta T}{R_4} + I_{bias} \right) \\
 &= \frac{1}{0.05} \cdot \left(\frac{1.5 \mu V + 3 \mu V + 30 nV/^\circ C \cdot 45^\circ C}{200 \Omega} + 300 pA \right) \quad (13) \\
 &= 591 nA
 \end{aligned}$$

As the operational amplifier functions as a follower and the input voltage noise is transferred directly to the output, the offset will appear directly over the current setting resistor. Input bias currents are drawn straight from the control current path and poached from the V_{load} input. We need the error contribution due to these effects to be less than 5% of the minimum step size. As R_4 decreases, the error contribution is decreased. We assume voltage errors due to bias currents are ignored as bias current compensation is applied, where resistance seen by the input ports of the amplifier is balanced.

The result means that the minimum step size can be set down to 591 nA without violating the accuracy requirements of the loadcell. This value can be further lowered by increasing the size of the current setting resistor.

A.3.2 Macro-cell - Dynamic Range

Upper limit of the dynamic current range is limited by the maximum control voltage and minimum load voltage.

$$I_{max} = \min \left(\frac{V_{control_{max}}}{R_7} \cdot \frac{R_3}{R_3 + R_6}, \frac{V_{load_{min}}}{R_7} \cdot \frac{R_3}{R_3 + R_6} \right), \quad (14)$$

This is similar as for the macro-cell, but here the effects of the control loop gain need to be accounted for as it is not unity unlike in the micro-cell. Like before though the minimum value is the control voltage of 2.5 V, yielding a maximum current of 250 mA with R_7 equal to 1 Ω . The contribution of errors to the minimum non-zero current step is the accuracy of the resistors, op amp supply rail voltage noise, offset voltage V_{OS} , offset drift V_D and input referred noise voltage V_N . The offset voltage and input referred noise of the feedback amplifier will be amplified by the gain in the feedback path. The offset voltage of IC_1 will not be amplified as it functions as a emitter follower. Assuming a 1 percent error in the lowest current supported, the minimum current supported, assuming a

target accuracy of 1 percent at the lowest current step, is approximated as:

$$\begin{aligned}
 I_{min} &= \frac{1}{E_{max}} \left(\frac{V_{N1} + V_{OS1} + V_{D1} \cdot \Delta T + \frac{R_3+R_6}{R_3} (V_{N2} + V_{OS2} + V_{D2} \cdot \Delta T)}{R_7} + I_b \right) \\
 &= \left(\frac{1.5 \mu V + 3 \mu V + 30 \text{ nV}/^\circ C \cdot 45^\circ C + \frac{113.3K\Omega}{11.3K\Omega} (1.5 \mu V + 3 \mu V + 30 \text{ nV}/^\circ C \cdot 45^\circ C)}{100 \cdot 1 \Omega} + 300 \text{ pA} \right) \\
 &= 6.45 \text{ mA},
 \end{aligned} \tag{15}$$

where I_b is the input bias current of the operational amplifier IC_2 and V_D is the drift voltage, respectively. ΔT is the maximum temperature difference from ambient. We assume voltage errors due to bias currents are ignored due to bias compensation being applied.

From the equation we see how we trade off the size of the resistor with the effect of error voltages on the current. Increasing the resistor decreases errors, but reduces minimum V_{load} .

Similarly as we increase the gain, to decrease $V_{load_{min}}$, the ratio of signal voltage to error voltage decreases.

The result indicates that 6.45 mA is the smallest current supported by the macro-cell, that fulfils the specification, assuming worst case error magnitudes.